J. Fluid Mech. (2018), *vol.* 837, *pp.* 19–47.
doi:10.1017/jfm.2017.817

Three-dimensional Rayleigh–Taylor instability under a unidirectional curved substrate

Gioele Balestra[1,†], Nicolas Kofman[1], P.-T. Brun[2,3], Benoit Scheid[4] and François Gallaire[1]

[1]Laboratory of Fluid Mechanics and Instabilities, EPFL, CH 1015 Lausanne, Switzerland

[2]Department of Mathematics, Massachusetts Institute of Technology, Cambridge, MA 02139, USA

[3]Department of Chemical and Biological Engineering, Princeton University, Princeton, NJ 08544, USA

[4]TIPs Laboratory, Université Libre de Bruxelles, C.P. 165/67, Avenue Franklin Roosevelt 50, 1050 Bruxelles, Belgium

(Received 9 June 2017; revised 25 September 2017; accepted 8 November 2017; first published online 19 December 2017)

We investigate the Rayleigh–Taylor instability of a thin liquid film coated on the inside of a cylinder whose axis is orthogonal to gravity. We are interested in the effects of geometry on the instability, and contrast our results with the classical case of a thin film coated under a flat substrate. In our problem, gravity is the destabilizing force at the origin of the instability, but also yields the progressive drainage and stretching of the coating along the cylinder's wall. We find that this flow stabilizes the film, which is asymptotically stable to infinitesimal perturbations. However, the short-time algebraic growth that these perturbations can achieve promotes the formation of different patterns, whose nature depends on the Bond number that prescribes the relative magnitude of gravity and capillary forces. Our experiments indicate that a transverse instability arises and persists over time for moderate Bond numbers. The liquid accumulates in equally spaced rivulets whose dominant wavelength corresponds to the most amplified mode of the classical Rayleigh–Taylor instability. The formation of rivulets allows for a faster drainage of the liquid from top to bottom when compared to a uniform drainage. For higher Bond numbers, a two-dimensional stretched lattice of droplets is found to form on the top part of the cylinder. Rivulets and the lattice of droplets are inherently three-dimensional phenomena and therefore require a careful three-dimensional analysis. We found that the transition between the two types of pattern may be rationalized by a linear optimal transient growth analysis and nonlinear numerical simulations.

Key words: instability, pattern formation, thin films

1. Introduction

The interface separating two fluids of different densities is subjected to the Rayleigh–Taylor instability (RTI) when the heavier fluid accelerates towards the lighter one (Rayleigh 1882; Taylor 1950; Sharp 1984). A classical description of the RTI for two semi-infinite domains can be found in Chandrasekhar (1981, chap. X).

† Email address for correspondence: gioele.balestra@epfl.ch

In particular, this instability occurs when a thin viscous fluid coats the underside of a substrate orthogonal to gravity. The occurrences of this phenomenon may be found in everyday life, when cooking, as condensed vapour arranges in a well-ordered pattern underneath a lid. Given the aspect ratio of such films, a lubrication approach is often used to describe their dynamics and thereby reduce the dimensionality of the problem: a two/three-dimensional problem can be described by a one/two-dimensional equation. One-dimensional linear stability analyses (Yiantsios & Higgins 1989; Limat 1993) indicate that the fluid's interface is asymptotically linearly unstable and that the most amplified perturbation has a wavelength of $\lambda_0 = 2\pi\sqrt{2}\ell_c$. The capillary length, $\ell_c = \sqrt{\gamma/\rho g}$, is defined, balancing the effect of surface tension γ and gravity ρg, where ρ is the film density. Fermigier *et al.* (1992) investigated the RTI of a thin layer of oil coated on the underside of a horizontal planar substrate and considered nonlinear effects as well. In the three-dimensional configuration, the fastest-growing patterns have circular and hexagonal symmetries. Additional complexity arises as the resulting pendent drops following the instability may pinch off or translate, collide and bounce (Limat *et al.* 1992; Lister, Rallison & Rees 2010), depending on the film thickness and the initial conditions.

Controlling and predicting the RTI is crucial to many engineering applications. In coating processes, the patterns resulting from the RTI may lead to undesired irregularities or even to the detachment of droplets for thick coatings. In toroidal nuclear fusion reactors, liquid metals coating the inside are used to protect the tokamak walls from the high-temperature plasma (Kaita *et al.* 2010). A droplet detaching and falling into the plasma could quench the process, with severe consequences. In oil-recovery applications, maximizing oil extraction is of paramount economic importance. In this context, the RTI in tubes might be a desirable feature, as it promotes a faster drainage of the film, as we shall discover in this paper. Similarly, interfacial instabilities have recently been seen in a new light and considered as a potential fabrication pathway to shape materials (Gallaire & Brun 2017). Desirable or not, the dynamics of the RTI in various configurations deserves to be understood.

A variety of stabilizing techniques have been explored in recent years, including the use of heat, vibrating substrates and electrical current (e.g. Burgess *et al.* 2001; Lapuerta, Mancebo & Vega 2001; Alexeev & Oron 2007; Weidner, Schwartz & Eres 2007; Weidner 2012; Cimpeanu, Papageorgiou & Petropoulos 2014). Babchin *et al.* (1983), considering the RTI between two fluids in a Couette flow, showed that the instability saturates as a consequence of the convective term in the evolution equation. A similar effect arises when the substrate is tilted (Oron & Rosenau 1989; Abdelall *et al.* 2006; Rohlfs, Pischke & Scheid 2017). Brun *et al.* (2015) have shown that dripping droplets can be avoided for sufficient inclinations, owing to the flow advection induced by the component of gravity parallel to the substrate. This stabilizing effect can be rationalized as a transition from an absolute to a convective instability (Brun *et al.* 2015; Scheid, Kofman & Rohlfs 2016). Likewise, the substrate curvature – such as that of a cylinder – suppresses the RTI if surface tension forces are strong enough (Trinh *et al.* 2014). Similarly to the tilted case, gravity acts not only as the destabilizing force at the origin of the instability (through its component perpendicular to the substrate) but also as a stabilizing force originating in the progressive drainage of the film (through its component parallel to the substrate). Furthermore, in the curved geometry, the increasing substrate inclination induces the stretching of the film. As a consequence, the interface is found to be asymptotically stable. Nonetheless, we have recently shown that such curved systems are still able to greatly amplify initial noise at short times

(Balestra, Brun & Gallaire 2016). Depending on the initial magnitude of the perturbation, the initial transient growth might be sufficiently large to trigger nonlinear effects resulting in three different regimes when solely considering a two-dimensional circular section of the cylinder: (i) no droplets, (ii) transient droplets eventually reabsorbed by the film and (iii) dripping droplets (Balestra *et al.* 2016). Contrasting with the RTI under a horizontal substrate, where there is no preferential direction for the instability (if boundaries are neglected) and a one-dimensional stability analysis suffices, the cylindrical substrate requires in principle a more intricate theoretical treatment. The dynamics in the polar and axial directions are different and a two-dimensional analysis has to be undertaken to consider the three-dimensionality of the problem (recall that the wall-normal direction has been averaged out into the lubrication approximation). Yet, as pointed out by Trinh *et al.* (2014), the dynamics of the RTI can be investigated by considering only the uppermost sector of the cylinder, which simplifies the theoretical treatment.

Here we undertake the analysis of a thin liquid film of initial average thickness H_i^* coating the inner side of a horizontal cylinder of radius R, extending the one-dimensional analyses of Trinh *et al.* (2014) and Balestra *et al.* (2016) to the remaining axial dimension. We show that allowing film perturbations along the axial direction can trigger various instability patterns, including drops and rivulets, which we explore experimentally, theoretically and numerically. The results of the linear optimal transient growth analysis, together with nonlinear numerical simulations, allow us to rationalize our experimental results. For moderate Bond numbers, $Bo = \rho g H_i^* R/\gamma$, a purely axial instability – yielding rivulets – arises. The liquid accumulates in equally spaced rivulets, similar to the rolls of Fermigier *et al.* (1992), yet with the significant difference that they persist over time as they drain out the film. For large Bond numbers, the instability pattern consists of droplets. These droplets form on a two-dimensional array similar to the one observed for the planar geometry (Fermigier *et al.* 1992), although the pattern in the curved geometry is stretched in the polar direction because of the draining flow.

The paper is structured as follows. The relevant dimensionless quantities are introduced in § 2.1. The experimental set-up is presented in § 2.2, followed by the description of the phase diagram in § 2.3. The linear optimal transient growth analysis is detailed in § 3. In particular, the governing equations are presented in § 3.1, linearized and solved analytically in § 3.2, and the results of the optimal transient growth analysis, described in § 3.3, are elucidated in § 3.4. Nonlinear effects on the pattern selection are investigated by performing two-dimensional simulations, which are presented in § 4. The draining rivulets are described in greater detail in § 5. The influence of the nonlinear interactions are discussed in § 5.1, whereas the experimental characterization of the rivulet dynamics is presented in § 5.2, followed by a numerical experiment of rivulet drainage in § 5.3.

2. Experimental results

2.1. *Relevant dimensionless parameters*

A thin viscous film of initial average thickness H_i^* coats the inside of a cylinder of inner radius R whose axis is orthogonal to gravity (figure 1). The film aspect ratio $\delta = H_i^*/R$ is small, $\delta \ll 1$. Defining μ as the dynamic viscosity, ρ the density and g the gravitational field, the drainage time is given by the gravitational relaxation scale $\tau_d = \mu R/(\rho g H_i^{*2})$ (Trinh *et al.* 2014). The other relevant time scale of the problem is that of the classic RTI, τ_{RT}, which is proportional to $\mu\gamma/(\rho^2 g^2 H_i^{*3})$

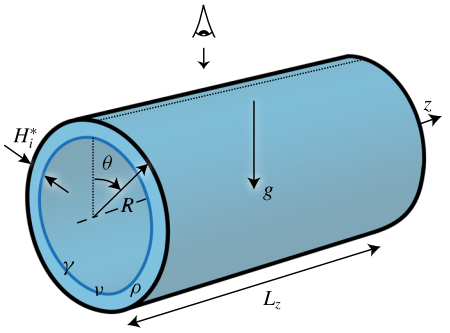

FIGURE 1. (Colour online) Sketch of the three-dimensional problem geometry.

(Fermigier *et al.* 1992), where γ is the fluid's surface tension. Taking the ratio between these two times, we define the Bond number as $Bo = \rho g H_i^* R/\gamma$, therefore accounting for the relative magnitude of gravitational and surface tension forces.

2.2. *Experimental set-up*

Experiments are performed with two types of silicone oil (Carl Roth GmbH) with kinematic viscosity $\nu = 1000$ cSt, density $\rho = 970$ kg m^{-3}, surface tension $\gamma = 21.2$ mN m^{-1} and $\nu = 5000$ cSt, $\rho = 973$ kg m^{-3}, $\gamma = 21.4$ mN m^{-1}, respectively. Two different techniques are adopted to obtain the initial uniform coating (see figure 2). The first one consists in using a poly(methyl methacrylate) (PMMA) cylinder partially filled with silicone oil and spinning it around its axis (see figure 2*a*). Following Melo (1993), the critical rotation velocity Ω_c above which a homogeneous film can be obtained is $\Omega_c = (A/4.428R)^2 g/\nu R$, where A is the cross-section of the cylinder occupied by the fluid. For $\Omega \gg \Omega_c$, the film thickness is expected to be uniform, so that the liquid is in solid-body rotation with the cylinder; whereas for $\Omega < \Omega_c$, different kinds of undesired instabilities can be observed (Thoroddsen & Mahadevan 1997; Hosoi & Mahadevan 1999; Pougatch & Frigaard 2011; Seiden & Thomas 2011). For the range of parameters under study, the threshold Ω_c is always less than 100 rpm, the speed at which we operate. Furthermore, for this speed, inertial instabilities such as the ones studied by Benilov & Lapin (2013) do not form in our experiments. The relative non-uniformity of the film thickness is within 2 %. After the uniform film is obtained, the rotation is suddenly stopped so that the coating stops too with time scale $\tau = H_i^{*2}/\nu$. Owing to the small film thickness and large viscosity, the time τ is small compared to the gravitational drainage time τ_d. More precisely, we get 0.4 ms $< \tau <$ 16 ms and 0.55 s $< \tau_d <$ 20.1 s, confirming $\tau \ll \tau_d$. We can therefore assume that the gravity-induced drainage starts from a uniform stationary condition.

For the second technique (see figure 2*b*), a uniform film of silicone oil is coated onto a planar PMMA plate with dimensions 500 mm $\times$ 200 mm $\times$ 4 mm using a film applicator (Film Casting Knife 15 cm, BYK GmbH), whose gap clearance can be tuned. The actual film thickness as well as its uniformity, which is within 4 %, are verified before proceeding. The film thickness is measured with a Confocal Chromatic Sensing technique (STIL CL2-MG140 and CL4-MG20 with CCS PRIMA), which allows measurements between 20 and 4000 µm, with an accuracy of 250 nm (see appendix E for further details on the measurement technique). After coating, the

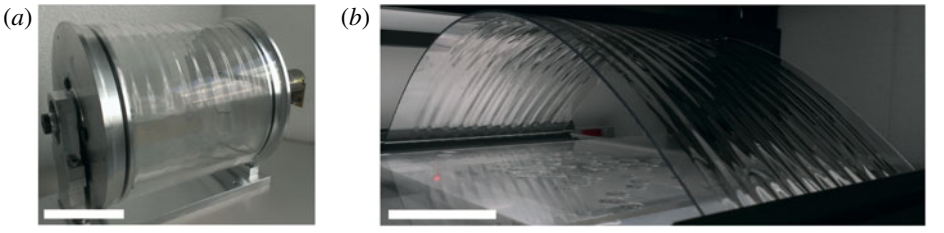

FIGURE 2. (*a*) Cylindrical substrate formed by a PMMA cylinder of radius $R = 8.6$ cm and length $L_z = 15$ cm partially filled with silicone oil. The axis of the cylinder is mounted on a motor which can reach 100 rpm for coating purposes. (*b*) Curved PMMA plate of 500 mm × 200 mm × 4 mm clamped at its extremities to prescribe the desired substrate curvature. The thin film of silicone oil is applied with a film applicator prior to deforming the plate. Scale bars correspond to 10 cm. Rivulets are visible in both photographs.

	Rotating cylinder	Curved plate
H_i^*	0.9–7.7 mm	0.11–2.04 mm
R	0.086 m	0.18–0.98 m
δ	1.1×10^{-2} to 9.3×10^{-2}	1.1×10^{-4} to 9.8×10^{-3}
Bo	35–308	37–349
τ_d	0.55–20.1 s	5.4 s to 2 h 10 min

TABLE 1. Values of relevant quantities for the experimentally explored parameter range.

plate is then turned upside down and bent by clamping its extremities. As a result, the upper part of the substrate – expected to be the key region – has a circular cross-section.

The achievable parameter range for each method is reported in table 1. As evident from the table, the rotating cylinder is suitable for intermediate Bond numbers and relatively large film aspect ratios, whereas the curved plate allows for a slightly wider range of Bond numbers and smaller aspect ratios owing to its flexibility in tuning the plate curvature.

A Basler camera (acA1300-60gm) with a long-focus zoom lens 18–108 mm $f/2.5$ (LMZ 45C5, Japan Lens Inc.) is employed to record the experiment. For the cylindrical set-up, we measured the temporal evolution of the film thickness at $\theta = 0$ along the cylinder length of $L_z = 15$ cm (see figure 1). The optical pen, measuring the film thickness at 200 Hz, is mounted on a linear motor stage (Aerotech PRO165LM), which performs oscillatory motions at 0.4 Hz. Given the slow dynamics induced by the high viscosity of the fluid, a sufficient temporal and spatial resolution (0.6 mm) is thus achieved.

2.3. *Phase diagram: rivulets or dripping droplets?*

In the classical RTI for horizontal substrates, thin films eventually destabilize into droplets, either directly or following the formation of rolls and axisymmetric structures caused by the presence of the contact line at the boundaries or local perturbations (Fermigier *et al.* 1992). The orientation of these structures is dictated only by the boundaries of the geometry or initial conditions. The fate of thin films coating the concave side of a cylindrical substrate is qualitatively different, as patterns such as

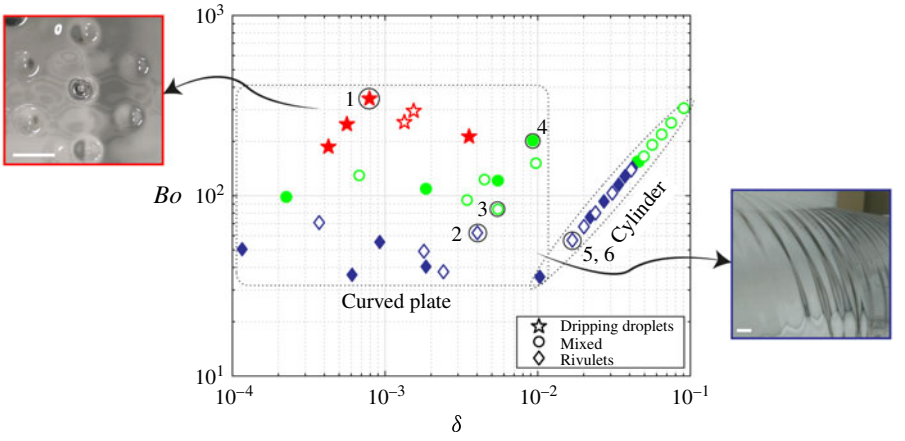

FIGURE 3. (Colour online) Phase diagram as a function of the film aspect ratio δ and Bond number Bo. Full symbols correspond to $\nu = 1000$ cSt and empty symbols to $\nu = 5000$ cSt. Numbers correspond to supplementary movies. The uncertainty on the film aspect ratio is of the order of 4 % (respectively 2 %) for the curved plate (respectively cylinder) set-up and the uncertainty on the Bond number is of the order of 5 %. Insets: top view of the two-dimensional hexagonal pattern of droplets (left) and side view of rivulets (right). Scale bars correspond to 10 mm.

rivulets may persist over time, i.e. drops do not necessarily form. Aiming to classify the patterns observed in our experiments, we have built a phase diagram that we report in figure 3. As evident from the figure, the diagram divides into three main regions, which we now describe.

Dripping droplets arise in the limit of very large Bond numbers ($Bo \gtrsim 200$) and vanishing film aspect ratios ($\delta < 10^{-2}$), that is, when the substrate may be seen as nearly horizontal on the scale of the film (see supplementary movie 1 available online at https://doi.org/10.1017/jfm.2017.817). Often, droplets arrange themselves on a hexagonal structure, as shown in the inset of figure 3. However, the initially formed two-dimensional array of droplets deforms over time following the drainage flow. Droplets were found to pinch off or slide along the substrate.

Rivulets are found for smaller Bond numbers, $Bo \lesssim 100$ (see figure 2 and supplementary movie 2), yet larger than the critical value, $Bo > 12$ (Trinh *et al.* 2014; Balestra *et al.* 2016). Unlike the rolls forming under a horizontal substrate, rivulets persist over time and do not further destabilize into droplets. These rivulets have a clear orientation dictated by the geometric anisotropy of the substrate curvature and are always orthogonal to the axis of the cylinder.

Dripping droplets and rivulets are separated by a mixed regime for Bond numbers of the order of 100, where both patterns coexist on the substrate: rivulets are typically found at the boundaries and droplets in the centre (see supplementary movie 3). For film aspect ratios $\delta > 7 \times 10^{-3}$, rivulets are found to experience a secondary instability at later times and destabilize into several aligned droplets which pinch off, similar to the pinch-off studied by Indeikina, Veretennikov & Chang (1997) and Alekseenko *et al.* (2015) (see supplementary movie 4).

Experiments performed with the cylinder display a larger critical Bond number for the transition from rivulets to the mixed regime. The main reason is the smoother initial film thickness in this configuration compared to the curved plate set-up. As will become clear in § 4, the system is very sensitive to ambient noise and particular

care has to be taken when performing the experiments. The thin-film evolutions in a cylinder for two different experiments with the same parameters are shown in supplementary movies 5 and 6, illustrating the reproducibility of the results.

In the phase diagram of figure 3, experiments with similar values of (Bo, δ) and different viscosities collapse to the same region. This is an indication that viscosity does not seem to play a major role in pattern selection, while it modifies the time scale for the appearance of such a pattern. Note that in our problem the typical time scale of the Rayleigh–Plateau instability (Hammond 1983; Duclaux, Clanet & Quéré 2006; Lister *et al.* 2006) is several orders of magnitude larger than the characteristic time of the classical RTI. In fact we have $\tau_{RP} \sim \mu(R - H_i^*)^4/(\gamma H_i^{*3}) \sim \mu R/(\gamma \delta^3)$ for the Rayleigh–Plateau instability and $\tau_{RT} \sim \mu \ell_c^4/(\gamma H_i^{*3})$ for the RTI, so that $\tau_{RP}/\tau_{RT} = (R/\ell_c)^4 \gg 1$. Furthermore, the dominant wavelength (see figure 2 or the inset of figure 3) is found to be proportional to the capillary length in our experiments as another indication of the relevance of the RTI. Recall that for the Rayleigh–Plateau instability the wavelength is proportional to the cylinder radius. We thus argue that rivulets form following the gravitational RTI.

Note finally that perturbations invariant in the axial direction, or waves, as studied in Trinh *et al.* (2014) and Balestra *et al.* (2016), are not observed in our experiments. In § 3 we propose a two-dimensional linear optimal transient growth analysis, for small aspect ratios, where we expect to identify the transition between rivulets and dripping droplets. Given the phase diagram in figure 3, we expect the value of the critical Bo to be independent of δ for $\delta \lesssim 10^{-2}$.

3. Linear optimal transient growth analysis

3.1. *Governing equation*

Owing to the small aspect ratio of the problem, $\delta \ll 1$, we use a lubrication approach to model the evolution of the film thickness (Oron, Davis & Bankoff 1997). Inertial effects are neglected due to the large viscosity of the fluid (the Reynolds number is of the order of 10^{-3}). The flow is driven by the gravitational field and by the capillary pressure gradient. By using the local mass conservation in cylindrical coordinates as well as H_i^* and τ_d as length and time gauges of the problem, the governing equation for the dimensionless film thickness $\bar{H}$ for small aspect ratios reduces to (see appendix A for more details on the derivation)

$$\bar{H}_t + \frac{1}{3}\left[\underbrace{\bar{H}^3}_{\mathrm{IV}}\left(\underbrace{\frac{1}{Bo}\bar{\kappa}_\theta}_{\mathrm{I}} + \underbrace{\delta \bar{H}_\theta \cos\theta}_{\mathrm{II}} + \underbrace{\sin\theta}_{\mathrm{III}}\right)\right]_\theta + \frac{1}{3\delta^2}\left[\underbrace{\bar{H}^3}_{\mathrm{IV}}\left(\underbrace{\frac{1}{Bo}\bar{\kappa}_z}_{\mathrm{I}} + \underbrace{\delta \bar{H}_z \cos\theta}_{\mathrm{II}}\right)\right]_z = 0, \tag{3.1}$$

where indices represent partial derivatives and $\bar{\kappa}$ is the curvature of the film interface. Terms I represent surface tension effects, terms II the variation of the hydrostatic pressure distribution, term III accounts for the gravity-induced drainage and term IV is the mobility of the liquid. The curvature up to the second order in δ is

$$\begin{aligned}\bar{\kappa} = {} & \frac{\bar{H}_{zz}}{(\bar{H}_z^2+1)^{3/2}} + \frac{\delta}{(\bar{H}_z^2+1)^{1/2}} \\ & - \delta^2\left[\frac{\bar{H}_{zz}\bar{H}_\theta^2}{2(\bar{H}_z^2+1)^{3/2}} - \frac{3\bar{H}_z^2\bar{H}_{zz}\bar{H}_\theta^2}{2(\bar{H}_z^2+1)^{5/2}} + \frac{2\bar{H}_z\bar{H}_{\theta z}\bar{H}_\theta}{(\bar{H}_z^2+1)^{3/2}} - \frac{\bar{H}_{\theta\theta}}{(\bar{H}_z^2+1)^{1/2}} - \frac{\bar{H}}{(\bar{H}_z^2+1)^{1/2}}\right] \\ & + O(\delta^3).\end{aligned} \tag{3.2}$$

Inspired by the good agreement between the linear optimal transient growth analysis of the top region of the cylinder (Trinh *et al.* 2014) with that of the entire circular geometry (Balestra *et al.* 2016), we concentrate on the cylinder's most unstable region close to $\theta = 0$. For $\delta \ll 1$, the change of variable $\theta = \delta^{1/2}x$ and $z = \delta^{-1/2}y$ is suitable. At leading order, the curvature reduces to $\bar{\kappa} = \delta(1 + \bar{H}_{xx} + \bar{H}_{yy})$. In the limit $x \ll 1$, the lubrication equation (3.1) becomes (see appendix B)

$$\bar{H}_t + \boldsymbol{\nabla} \cdot \left[\frac{\bar{H}^3}{3} \boldsymbol{\nabla} \left(\frac{1}{Bo} \nabla^2 \bar{H} + \bar{H} + \underbrace{\frac{x^2}{2}}_{\text{III}} \right) \right] = 0, \tag{3.3}$$

where $\boldsymbol{\nabla} = [\partial_x, \partial_y]^{\mathrm{T}}$ is the gradient operator. Equation (3.3) differs from the classical lubrication equation employed for the horizontal substrate (Fermigier *et al.* 1992) only by the presence of the drainage term III. This term breaks the symmetry of the problem and is the key to the following analysis.

3.2. *Linear disturbance solution*

For a uniform film thickness, $\bar{H}(x, y, t) = H(t)$, (3.3) has an analytical solution of the form (Takagi & Huppert 2010; Trinh *et al.* 2014; Lee *et al.* 2016)

$$H(T) = \frac{1}{\sqrt{T}}, \tag{3.4}$$

with $T = 1 + (2/3)t$ (see appendix C for the derivation). This solution will be shown to be asymptotically stable and we will refer to it as the drainage solution.

The film thickness is decomposed into this spatially uniform drainage solution $H(T)$ and small space-dependent disturbances $\varepsilon h(x, y, T)$:

$$\bar{H}(x, y, T) = H(T) + \varepsilon h(x, y, T), \quad \varepsilon \ll 1. \tag{3.5}$$

Entering the decomposition (3.5) into the lubrication equation (3.3) and considering first-order terms, we obtain the linear disturbance equation for the perturbations:

$$h_T + \frac{1}{2T^{3/2}} \left(\frac{\nabla^4 h}{Bo} + \nabla^2 h \right) + \frac{3}{2T}(x h_x + h) = 0. \tag{3.6}$$

In this expression, the base flow H is explicitly accounted for by the powers of T. For an initially harmonic disturbance $h(x, y, 1) = h_0(x, y) = \exp[\mathrm{i}(\alpha x + \beta y)] + \text{c.c.}$ with wavenumber α in the polar direction and β in the axial direction, the solution is

$$h(x, y, T) = A(\alpha, \beta, T) \exp\left[\mathrm{i} \left(\alpha \frac{x}{T^{3/2}} + \beta y \right) \right] + \text{c.c.}, \tag{3.7}$$

where A satisfies

$$A_T + \frac{1}{2} \left[\frac{1}{Bo} \left(\frac{\alpha^4}{T^{15/2}} + \frac{\beta^4}{T^{3/2}} + 2\frac{\alpha^2\beta^2}{T^{9/2}} \right) - \left(\frac{\alpha^2}{T^{9/2}} + \frac{\beta^2}{T^{3/2}} \right) + \frac{3}{T} \right] A = 0. \tag{3.8}$$

The temporal dependence of the apparent wavenumber in the polar direction, $x/T^{3/2}$, is chosen so as to annihilate the stretching term $x h_x$ in (3.6). The solution

$$A(\alpha,\beta,T) = \frac{1}{T^{3/2}}\exp\left[\left(1-\frac{1}{T^{7/2}}\right)\frac{\alpha^2}{7}-\frac{1}{Bo}\left(1-\frac{1}{T^{13/2}}\right)\frac{\alpha^4}{13}+\left(1-\frac{1}{T^{1/2}}\right)\beta^2-\frac{1}{Bo}\left(1-\frac{1}{T^{1/2}}\right)\beta^4-\frac{1}{Bo}\left(1-\frac{1}{T^{7/2}}\right)\frac{2\alpha^2\beta^2}{7}\right] \tag{3.9}$$

is composed of two parts. On the one hand, the exponential term results from the RTI, with both destabilizing terms in α^2 or β^2 and stabilizing terms in α^4, β^4 or $\alpha^2\beta^2$. This exponential term saturates to a maximal amplitude due to the thinning of the film, accounted for by the powers of T. The largest amplitude depends only on the wavenumbers and on the Bond number. On the other hand, the gravity-induced drainage also enters through the algebraic term $1/T^{3/2}$, which eventually makes the amplitude vanish for large times, $\lim_{T\to\infty} A(\alpha,\beta,T)=0$. In view of (3.9), it is therefore clear that the system is linearly asymptotically stable and only a transient growth can be achieved.

The initial amplitude evolution is given by

$$A(\alpha,\beta,T\to 1)\sim 1+\frac{(\alpha^2+\beta^2-3)Bo-(\alpha^2+\beta^2)^2}{2Bo}(T-1)+O[T-1]^2. \tag{3.10}$$

Introducing the oblique mode $\boldsymbol{k}=\alpha\,\boldsymbol{e}_x+\beta\,\boldsymbol{e}_y$, with norm $k=\sqrt{\alpha^2+\beta^2}$, initial growth occurs only if $k^2-3-k^4/Bo>0$. This condition is best met for

$$k_0=\sqrt{Bo/2}, \tag{3.11}$$

which is the initially most amplified wavenumber. In agreement with Trinh *et al.* (2014) and Balestra *et al.* (2016), we thus recover the condition $Bo>12$. We conclude that the threshold of the initial growth is not dependent on perturbation direction and the wavenumber k_0 corresponds to the wavenumber with the largest linear growth in the planar RTI (Fermigier *et al.* 1992).

In our formalism, waves and rivulets correspond to modes with $\boldsymbol{k}=\alpha\,\boldsymbol{e}_x$ and $\boldsymbol{k}=\beta\,\boldsymbol{e}_y$, respectively. The time evolution of the amplitude of waves and rivulets for the initial wavenumber of norm k_0 are shown in figure 4 for different Bond numbers. The growth of rivulets is much stronger than that of waves, and they persist longer, thereby rationalizing why waves are never seen in experiments. Note that waves and rivulets are the two limiting cases, as more generic perturbations can be expressed as a linear combination of α and β such that $\boldsymbol{k}=\alpha\,\boldsymbol{e}_x+\beta\,\boldsymbol{e}_y$.

3.3. *Optimal growth*

The optimization of the perturbations modes is performed for pure α and pure β modes separately. The optimal wavenumbers and the optimal times correspond to the wavenumbers and times for which the amplitude is the largest.

Following (3.9) we find that the optimal wavenumber for the waves is

$$\left.\frac{\partial A}{\partial\alpha}\right|_{\beta=0}=0 \quad\Longleftrightarrow\quad \alpha_{max}(T)=\sqrt{\frac{13}{14}\frac{(1-T^{-7/2})}{(1-T^{-13/2})}Bo}, \tag{3.12}$$

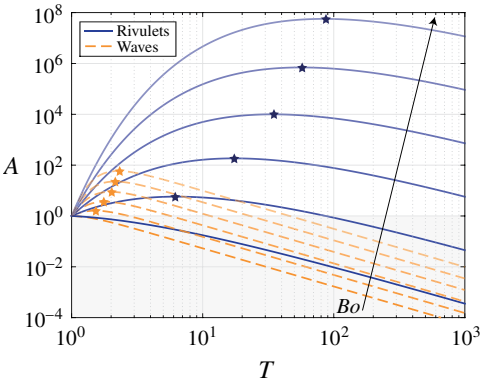

FIGURE 4. (Colour online) Linear perturbative results. The amplitude A is shown for waves ($\beta = 0$) and rivulets ($\alpha = 0$). They correspond to an initial perturbation with $k = k_0$ (see (3.11)) for Bond numbers $Bo = 10$, 30, 50, 70, 90 and 110. Stars denote the largest amplitudes.

whereas for the rivulets it is

$$\left.\frac{\partial A}{\partial \beta}\right|_{\alpha=0} = 0 \quad \Longleftrightarrow \quad \beta_{max} = \sqrt{\frac{Bo}{2}}. \tag{3.13}$$

Hence, the wavenumber for the rivulets to reach the largest growth at any time always corresponds to the classical RTI most amplified wavenumber k_0. The optimal wavenumber for waves has a weak dependence on the optimization time and tends to $k_0\sqrt{13/7}$ for large time horizons (see inset in figure 5*a*). The largest growths reached by waves and rivulets as a function of time are therefore

$$A_{\alpha_{max}}(T) = A(\alpha_{max}, 0, T) = \frac{1}{T^{3/2}} \exp\left[\frac{13}{196}\frac{\left(1 - T^{-7/2}\right)^2}{\left(1 - T^{-13/2}\right)} Bo\right], \tag{3.14}$$

$$A_{\beta_{max}}(T) = A(0, \beta_{max}, T) = \frac{1}{T^{3/2}} \exp\left[\frac{1}{4}(1 - T^{-1/2}) Bo\right]. \tag{3.15}$$

Solving $\partial A_{\alpha_{max}}/\partial T = 0$ and $\partial A_{\beta_{max}}/\partial T = 0$ yields the times at which the amplitude is the largest. For rivulets, one finds $T_{A^{\beta}_{max}} = (Bo/12)^2$ and the largest linear transient growth of rivulets is thus

$$A^{\beta}_{max} = \left(\frac{12}{Bo}\right)^3 \exp\left(\frac{1}{4}Bo - 3\right). \tag{3.16}$$

The time optimization for waves yields an irreducible polynomial of degree 25 that does not have an algebraic solution. The numerical solution shows that $T_{A^{\alpha}_{max}}$ follows a power law with exponent close to 0.2 for the considered Bond-number range. The largest linear transient growth that the waves can achieve for large Bond numbers scales as

$$A^{\alpha}_{max} \sim \exp\left(\frac{13}{196}Bo\right) \quad \text{for } Bo \gg 12. \tag{3.17}$$

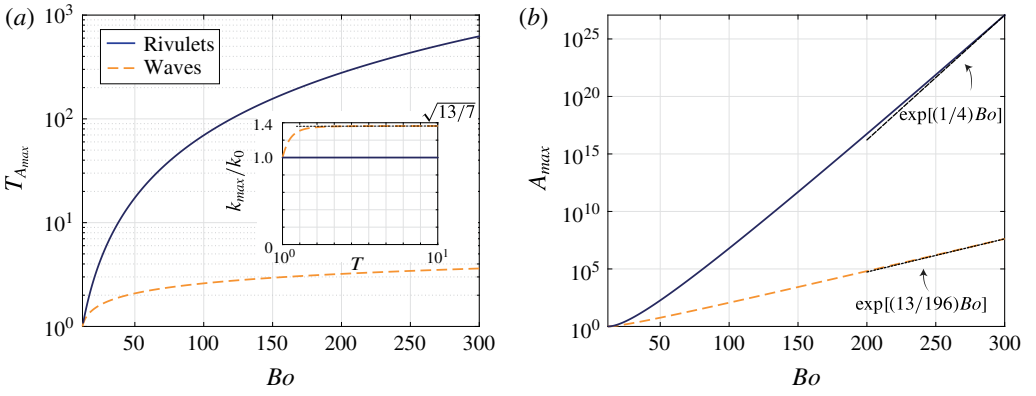

FIGURE 5. (Colour online) (*a*) Times $T_{A_{max}} = \{T_{A^{\alpha}_{max}}, T_{A^{\beta}_{max}}\}$ corresponding to the largest amplitude $A_{max} = \{A^{\alpha}_{max}, A^{\beta}_{max}\}$ obtained by perturbing with the optimal wavenumbers $k_{max} = \{\alpha_{max}, \beta_{max}\}$ as a function of the Bond number. Inset: optimal wavenumbers rescaled by the horizontal RTI wavenumber k_0 as a function of time. (*b*) Largest achievable amplitudes A_{max} as a function of the Bond number. Black dashed lines correspond to the high-Bond-number limit evolutions. Note that the disturbance amplitude εA needs to be smaller than the base flow of order unity for the linear theory to hold.

The optimal times, as well as the corresponding largest amplitudes, are reported in figure 5. This optimization procedure confirms what has been observed in figure 4. The optimal times and amplitudes of the rivulets are much greater than those of the waves. Waves are stretched by the draining flow, see (3.7), reducing the time available for the instability to grow. The stretching effect is evidenced by the different temporal evolutions of the stabilizing and destabilizing RTI terms in (3.9). In contrast, rivulets only experience the thinning of the film, without being stretched along their characteristic direction. They grow for longer times and therefore reach larger amplitudes.

3.4. *Linear prediction*

Equipped with the results of the linear optimal transient growth (summarized in table 2), we aim to better understand our experimental results. In particular, we consider the linear evolution of rivulets, $h_0(x, y) = \exp(\mathrm{i}k_0 y) + \text{c.c.}$, waves, $h_0(x, y) = \exp(\mathrm{i}k_0 x) + \text{c.c.}$, and hexagons having one vector aligned with the axis of the cylinder,

$$h_0(x, y) = \tfrac{1}{3}\{\exp(\mathrm{i}k_0 y) + \exp[\mathrm{i}(\tfrac{1}{2}\sqrt{3}k_0 x - \tfrac{1}{2}k_0 y)] + \exp[\mathrm{i}(-\tfrac{1}{2}\sqrt{3}k_0 x - \tfrac{1}{2}k_0 y)]\} + \text{c.c.}, \tag{3.18}$$

with $\alpha = \beta = k_0$ the initially most amplified wavenumber, and we choose an initial perturbation with amplitude $\varepsilon = 10^{-3}$. The linear theory holds as long as the magnitude of the disturbances εA is smaller than the base flow, which is of order unity; see (3.5).

We find that, for low Bond numbers, $Bo \simeq 60$, rivulets experience a linear growth strong enough for the perturbation to become of the order of the base flow (see figure 6*a*), while the waves remain much smaller. The hexagons experience a large linear growth since they contain a rivulet mode. However, their amplitude remains smaller than one-third of that of the rivulets. For larger Bond numbers, e.g. $Bo = 160$

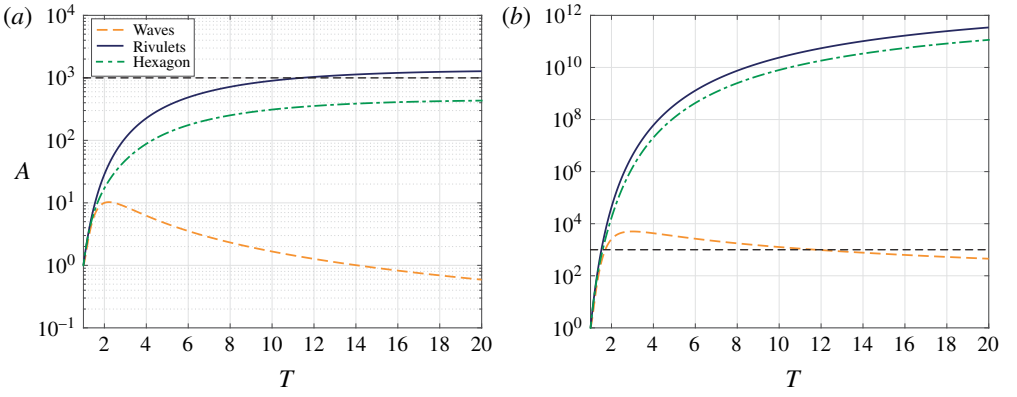

FIGURE 6. (Colour online) Amplitude evolution of rivulets, waves and hexagons for (*a*) $Bo = 60$ and (*b*) $Bo = 160$. Thin dashed lines indicate necessary amplification of disturbances to become of order one when $\varepsilon = 10^{-3}$. Given the asymptotic stability of the system, the amplitude of all initial conditions saturates and tends to zero for large times, which is the reason why only the evolution for $T \leqslant 20$ is presented here.

	Optimal wavenumber	Optimal time	Optimal gain ($Bo \gg 12$)
Waves	$\alpha_{max}(T) = \sqrt{\frac{13}{14}\frac{(1-T^{-7/2})}{(1-T^{-13/2})}Bo}$	$T_{A^{\alpha}_{max}} \sim Bo^{0.2}$	$A^{\alpha}_{max} \sim \exp\left(\frac{13}{196}Bo\right)$
	$\alpha_{max}(T \to 1) = \sqrt{\frac{Bo}{2}}$,		
	$\alpha_{max}(T \to \infty) = \sqrt{\frac{13Bo}{14}}$		
Rivulets	$\beta_{max} = \sqrt{\frac{Bo}{2}}$	$T_{A^{\beta}_{max}} = \left(\frac{Bo}{12}\right)^2$	$A^{\beta}_{max} \sim \exp\left(\frac{1}{4}Bo\right)$

TABLE 2. Summary of main results of the linear optimal transient growth analysis.

in figure 6(*b*), rivulets, hexagons as well as waves experience a similar linear growth up to the amplitude where nonlinear effects become relevant. Thereby, for sufficiently large Bond numbers, the instability pattern is selected only by the nonlinear effects. Conversely, linear growth selects the pattern for low Bond numbers. Note that the critical Bond number at which nonlinear effects enter into play before the linear growth has promoted a specific pattern is dependent on perturbation amplitude. The experimental threshold of $Bo \sim 100$, corresponding to the mixed regime of figure 3, is related to our experimental settings.

4. Nonlinear two-dimensional simulations

We have seen in § 3.4 that the linear stability analysis is sufficient to predict the occurrence of rivulets is some cases (low Bond numbers), but does not allow us to conclude anything about the fate of perturbations in other cases (large Bond numbers).

Fermigier *et al.* (1992) performed a weakly nonlinear analysis for the horizontal RTI. In particular, they showed that the fundamental mode of rolls, which correspond to rivulets for the planar geometry, is stabilized by the nonlinear interaction with the first harmonic of the perturbations. This interaction modifies the amplitude of the rolls only at order ε^3. Furthermore, they have also shown that a two-dimensional pattern of hexagons is amplified at second order through the interactions between fundamental modes oriented at 120° to each other, like the one of (4.1). This pattern typically appears when the instability's vertical symmetry is broken (Fauve 2005; Lister *et al.* 2010), meaning that the equations are not invariant under a change of sign for h. In our context, these nonlinear effects could explain the predominance of a two-dimensional array of droplets instead of rivulets for large Bo. However, although the weakly nonlinear expansion of Fermigier *et al.* (1992) suggests the right stabilizing/destabilizing nonlinear effects, the expansion is not convergent and can be used only for $t \to 0$ when ε gets larger.

Here, such a truncated weakly nonlinear expansion is even more delicate in view of the draining flow in the polar direction, which stretches the wavenumbers. As a consequence, we instead propose to use two-dimensional numerical simulations of (3.1) so as to investigate nonlinear effects in two-dimensional initial disturbances (see appendix D.1 for details on the numerical methods). The computational domain is $\theta \in [-\pi, \pi]$ and $z \in [-4\pi/b_0, 4\pi/b_0]$. We consider the most amplified pattern for the classic RTI with wavenumbers in the (θ, z)-space $a_0 = k_0\delta^{-1/2} = \sqrt{Bo/2\delta}$ and $b_0 = k_0\delta^{1/2} = \sqrt{Bo\delta/2}$, and set the initial condition to be

$$\bar{H}_0 = 1 + \varepsilon\{\cos(b_0 z) + \cos[-\tfrac{1}{2}b_0 z + \tfrac{1}{2}\sqrt{3}a_0(\theta+\phi)] + \cos[-\tfrac{1}{2}b_0 z - \tfrac{1}{2}\sqrt{3}a_0(\theta+\phi)]\}. \tag{4.1}$$

The initial condition is chosen to be aligned with z and shifted by ϕ along the polar direction to avoid symmetry at $\theta = 0$.

The results for several values of ε and $\phi = 0.02$ are shown in figure 7. They correspond to the same Bond number, $Bo = 100$. As evident from the figure, different patterns arise depending on the initial perturbation amplitude. Rivulets are found to form for small ε, despite the imposed hexagonal initial condition. However, when the perturbation is large, the two-dimensional pattern of hexagons grows and dominates the dynamics. Note an intrinsic limitation of our model: owing to the use of the lubrication equation, we do not account for pinching-off drops, which may arise at longer times. Given the amplifying nature of this system (see table 2), the same result is obtained by fixing the disturbance amplitude and varying the Bond number (see figure 8).

It has to be stressed that the finally observed pattern is not dependent on the structure of the initial condition. If random noise is imposed as initial condition, rivulets will still appear at low Bond numbers and a two-dimensional pattern of isolated droplets will form at large Bond numbers (see figure 9). The randomness of the initial condition limits the nonlinear interactions and pushes the critical Bo as well as the pattern-formation time to larger values.

The transition from rivulets to a two-dimensional pattern is in agreement with what has been obtained experimentally and presented in § 2.3. Rivulets dominate at low Bond numbers whereas nonlinear interactions select the pattern from linearly equally growing modes at larger Bond numbers. Numerical results show that this transition can be triggered similarly by varying disturbance amplitudes, which is difficult to check experimentally. Nonlinear two-dimensional simulations complete

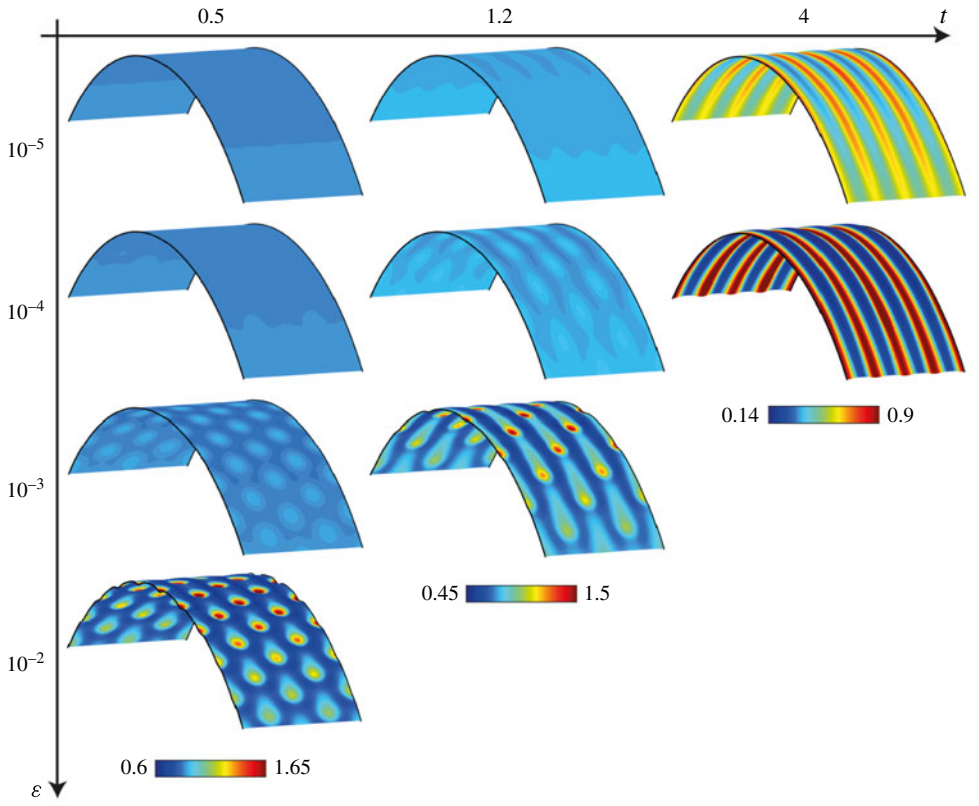

FIGURE 7. (Colour online) Numerical results of nonlinear two-dimensional simulation. Evolution of the film thickness for a similar initial hexagonal condition (4.1) with amplitude $\varepsilon = 10^{-5}$, 10^{-4}, 10^{-3} and 10^{-2} at times $t = 0.5$, 1.2 and 4 for $Bo = 100$ and $\delta = 0.01$. The angular shift is $\phi = 0.02$. Only the uppermost area in the sector $z \in [-4\pi/b_0, 4\pi/b_0]$ and $\theta \in [-\pi/4, \pi/4]$ is shown.

the analysis of the pattern selection for the three-dimensional RTI under a curved substrate. While rivulets are mainly selected by linear effects along the axial direction, the two-dimensional pattern of droplets relies solely on nonlinear interactions.

5. Characterization of the rivulets

5.1. *Nonlinear simulations at the top of the cylinder*

In order to gain more insight into the dynamics of the rivulets, numerical simulations of the one-dimensional lubrication equation for the film thickness at the top of the cylinder are carried out ($\theta = 0$). The lubrication equation (3.1) at $\theta = 0$ with vanishing polar derivatives reads

$$\bar{H}_t + \underbrace{\frac{1}{3}\bar{H}^3}_{\mathrm{I}} + \underbrace{\frac{1}{3\delta^2}\left[\bar{H}^3\left(\frac{1}{Bo}\bar{\kappa}_z + \delta\bar{H}_z\right)\right]_z}_{\mathrm{II}} = 0. \tag{5.1}$$

The term labelled I results from the drainage term in (3.1) and is responsible for the thinning of the film over time. The terms labelled II match the classical terms of the

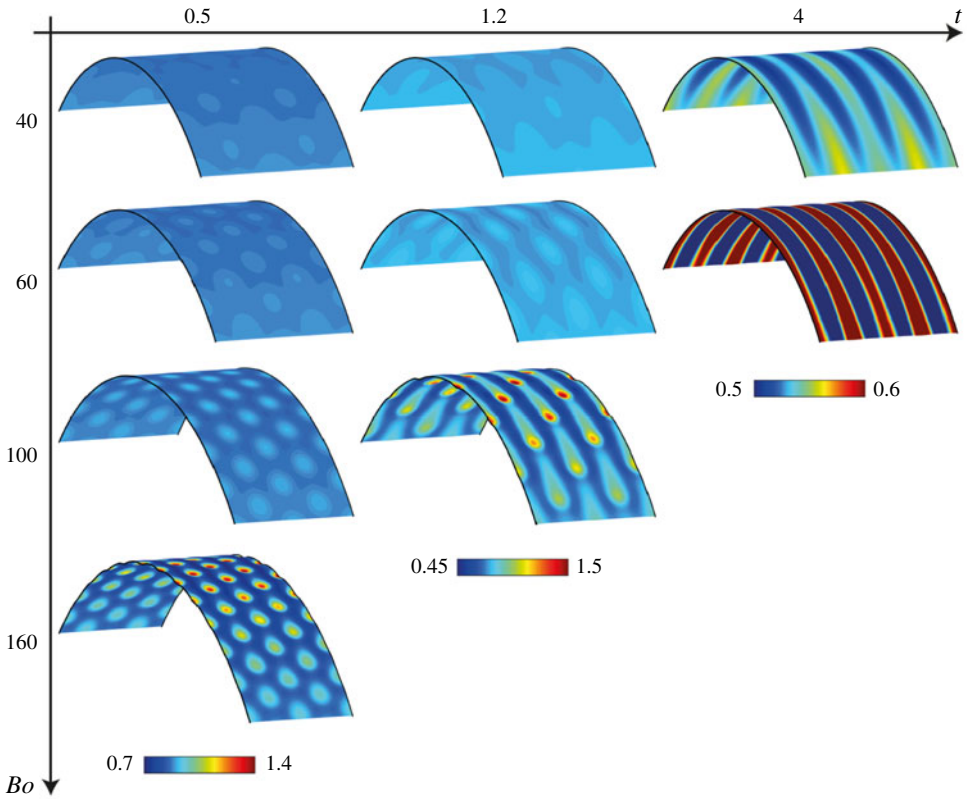

FIGURE 8. (Colour online) Numerical results of nonlinear two-dimensional simulation. Evolution of the film thickness for a similar initial hexagonal condition (4.1) with amplitude $\varepsilon = 10^{-3}$ at times $t = 0.5$, 1.2 and 4 for $Bo = 40$, 60, 100, 160 and $\delta = 0.01$. The angular shift is $\phi = 0.02$. Only the uppermost area in the sector $z \in [-4\pi/b_0, 4\pi/b_0]$ and $\theta \in [-\pi/4, \pi/4]$ is shown. If one fixes the initial film thickness and the cylinder radius, increasing Bo reduces to increasing the most amplified wavenumber in the axial direction $b_0 = \sqrt{Bo\delta/2}$, i.e. to decreasing the capillary length.

equation describing the classical horizontal RTI (Fermigier *et al.* 1992). Equation (5.1) can be resolved numerically (see appendix D.2 for details) and its solution is validated by comparison with a two-dimensional nonlinear numerical simulation in figure 10(*b*). The domain size is $L_z = 2 \times 2\pi/b_0$, with $b_0 = k_0\delta^{1/2} = \sqrt{Bo\delta/2}$ the linear optimal wavenumber in the physical z-space and the initial condition is $\bar{H}_0 = 1 + \varepsilon\cos(b_0 z)$. Periodic boundary conditions are used. An example of nonlinear evolution given by (5.1) is presented in figure 10. The narrow rivulets, whose peaks grow initially in time, are separated by a rather flat thin-film region (see figure 10*b*).

The nonlinear perturbation solution is given by $h(z, t) = [\bar{H}(z, t) - H(t)]/\varepsilon$, where $H(t) = (1 + 2t/3)^{-1/2}$ is the drainage solution at $\theta = 0$ introduced in (3.4) and $\bar{H}(z, t)$ is obtained by the numerical resolution of (5.1). The amplitudes of the different harmonics can be found by the Fourier series decomposition of the perturbation h:

$$h(z, t) = \sum_{n\in\mathbb{N}} A_n(t)\exp(\mathrm{i}nb_0 z) + \text{c.c.} \tag{5.2}$$

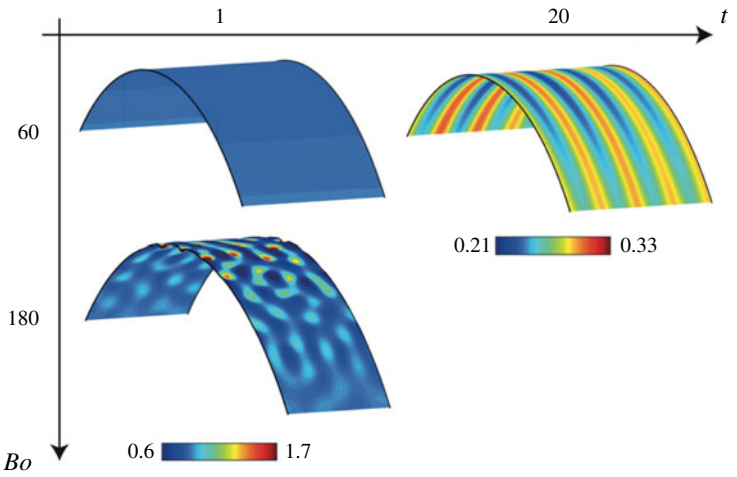

FIGURE 9. (Colour online) Numerical results of nonlinear two-dimensional simulation. Evolution of the film thickness for a random-noise initial condition with maximal amplitude $\varepsilon = 5 \times 10^{-4}$ at times $t = 1$ and 20 for $Bo = 60$ and 180 and $\delta = 0.01$. Only the uppermost area in the sector $z \in [-4\pi/b_0, 4\pi/b_0]$ and $\theta \in [-\pi/4, \pi/4]$ is shown, with $b_0 = \sqrt{Bo\delta/2}$.

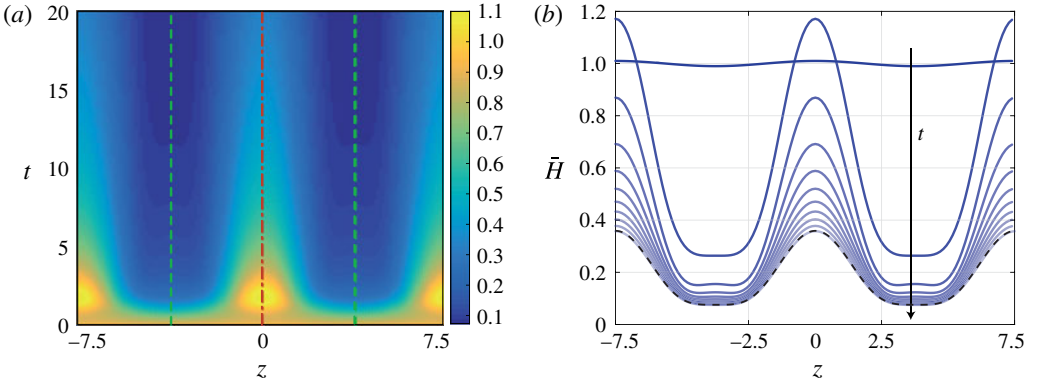

FIGURE 10. (Colour online) Nonlinear simulations at $\theta = 0$, i.e. using (5.1). Film thickness as a function of time for rivulets with optimal initial disturbance $\bar{H}_0 = 1 + 0.01\cos(b_0 z)$ with $b_0 = \sqrt{Bo\delta/2}$. (*a*) Spatio-temporal map of the film thickness $\bar{H}$. Dash-dotted and dashed lines correspond to the locations of the peaks and valleys, respectively, whose thickness evolution is shown in figure 12(*a*). (*b*) Profiles of $\bar{H}$ at successive times $t = 0, 2, \ldots, 20$. The black dashed line corresponds to the nonlinear solution at $\theta = 0$ and $t = 20$ obtained when considering the entire circular geometry $-\pi < \theta < \pi$, equation (3.1). Here $Bo = 70$ and $\delta = 0.02$.

Results are presented in figure 11(*a*). The fundamental mode, A_1, obtained via nonlinear simulations agrees well with our linear prediction for small values of ε. Nonetheless, for larger initial perturbations, A_1 is found to saturate and to subsequently decrease well before the linear prediction A does. Albeit $\|A\|_2$ and A_1 mostly agree, that is, A_0 and higher harmonics do not contribute significantly

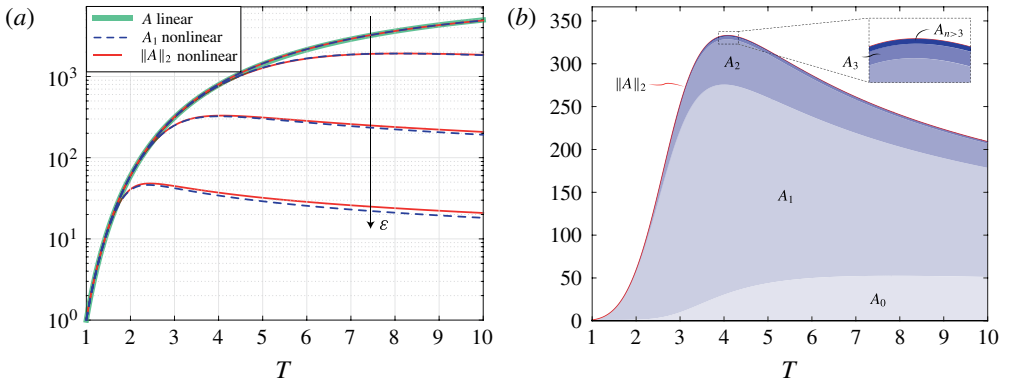

FIGURE 11. (Colour online) (*a*) Linear (green solid line) and nonlinear (blue dashed lines) amplitudes of the fundamental, together with the total nonlinear amplitude (red solid lines) for the optimal initial disturbance $\bar{H}_0 = 1 + \varepsilon \cos(b_0 z)$ with $b_0 = \sqrt{Bo\delta/2}$ and different initial disturbance amplitudes $\varepsilon = 10^{-5}$, 10^{-4}, 10^{-3} and 10^{-2}. Here $Bo = 70$ and $\delta = 0.02$. (*b*) Evolution of the total nonlinear disturbance energy $\|A\|_2$ together with the relative amplitude of the different harmonics A_n of (5.2). Here $\varepsilon = 10^{-3}$, $Bo = 70$ and $\delta = 0.02$.

to the energy, as evident from figure 11(*b*), we argue that their interaction with A_1 generates the observed saturation and therefore cannot be neglected. This type of stabilizing effect is in agreement with the aforementioned analysis of Fermigier *et al.* (1992) for rolls. Note that, the larger the initial disturbance amplitude, the earlier the higher harmonics will influence the dynamics of the fundamental mode. Yet, if the amplitude is sufficiently small, the transient growth nature of the instability guarantees that the linear prediction holds for all times (not shown in figure 11(*a*), the linear evolution remains superimposed on the nonlinear evolution for $\varepsilon = 10^{-5}$ and $T > 10$). The perturbation amplitude saturates and eventually vanishes due to the asymptotic stability of the system.

Despite their small contribution to $\|A\|_2$, the higher-order harmonics are visible in our system. In figure 10(*b*), one can see that the flat regions between two fundamentals are subject to an instability too. This phenomenon is akin to the cascade of structures observed by Boos & Thess (1999) for the Marangoni instability in a thin film.

Our nonlinear analysis also indicates a modification in the base flow. We found that the mean film thickness of the perturbed film is smaller than the one of the draining solution $H(t) = 1/\sqrt{1 + 2t/3}$ (Takagi & Huppert 2010; Trinh *et al.* 2014; Lee *et al.* 2016) (see figure 12*a*). The development of rivulets hastens the drainage, which results from the coupling between the shape of the rivulets and the strong variation in the mobility of the liquid that scales as the cube of the local thickness, see (3.1). Initially, the different components of the thickness follow the linear evolution. There is no correction of the drainage solution due to the rivulets at early times. Nonetheless, when the higher harmonics come into play, A_0 is no longer vanishing (see figure 11*b*). Building upon this observation, forcing the formation of rivulets is advantageous if one wishes to accelerate the drainage. Similar effects exist when waves run down at the surface of a liquid film flowing down an inclined plane (Kofman, Ruyer-Quil & Mergui 2016). Such a modification of the mean flow is also a key to the saturation of hydrodynamic instabilities like vortex shedding in the wake flow behind a cylinder (Maurel, Pagneux & Wesfreid 1995; Mantič-Lugo, Arratia & Gallaire 2014).

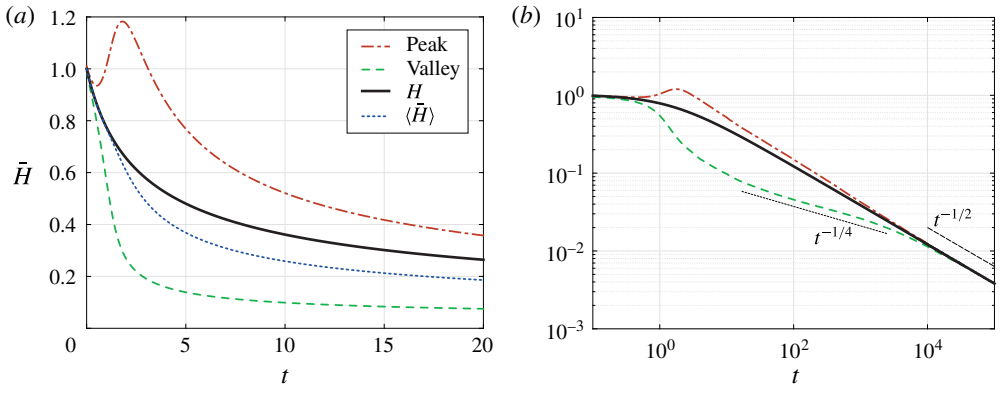

FIGURE 12. (Colour online) (*a*) Film thickness evolutions at the peaks (red dash-dotted line) and valleys (green dashed line) of the rivulets shown in figure 10. The thick black solid line corresponds to the pure drainage solution H and the blue dotted line to the mean film thickness $\langle\bar{H}\rangle$. (*b*) Long-time evolutions for peaks, valleys and the pure drainage solution. Here $Bo = 70$, $\delta = 0.02$ and $\varepsilon = 10^{-2}$.

Moving away from the mean value of the film thickness, we now describe the evolution of the film thickness evolution in the peaks and valleys shown in figure 12. The growth of the peaks is fed by liquid extracted from the valleys. This mechanism is similar to the rolls in the planar RTI (Fermigier *et al.* 1992; Weidner, Schwartz & Eres 1997; Lister *et al.* 2010) or to the collars in the instability of a thin annular film coating the inside or outside of a cylinder in the absence of gravity (Hammond 1983; Lister *et al.* 2006). However, due to the thinning of the film in time, rivulets can only grow at short times. At later stages, the film thins and thus limits the liquid that a rivulet can pull from its vicinity. We find that, before the film becomes uniform again, the thickness in the valleys follow the scaling $t^{-1/4}$ (see figure 12*b*). The same scaling was found by Lister *et al.* (2010) for thin regions between pendent drops below planar substrates and for the lobes inside a cylinder studied by Hammond (1983). At these intermediate times, the drainage of the rivulet valleys is driven by the classical RTI term II in (5.1), yielding $\bar{H} \sim t^{-1/4}$, as the effect of the term I is negligible. For peaks, the term I of (5.1) is not negligible, as the film thicknesses $\bar{H}$ is relatively larger. Eventually, the film thickness becomes uniform again due to the drainage in the rivulets and the drainage scales like the base flow, $\bar{H} \sim t^{-1/2}$.

5.2. *Experimental measurements*

Rivulets are characterized experimentally by measuring the film thickness at the top of the cylinder. The spatio-temporal film thickness map is shown in figure 13(*a*). Rivulets first form at the boundaries of the cylinder where the film is perturbed by the existence of a meniscus. They then progressively invade the entire domain (see figure 13*b*). As time evolves, the thickness of the rivulets eventually decreases, but their structure does not destabilize and we do not see any drops forming.

The rivulets were found to be almost equally spaced in experiments, with wavelength $\lambda = 14 \pm 1$ mm. The linearly most amplified wavelength is $\lambda^{\beta}_{max} = 2\pi/\sqrt{Bo\,\delta/2}H^*_i = 13.5$ mm (see § 3.3). Keeping in mind that the calculation leading to this value is idealized – infinite domain approximation – we find that the agreement

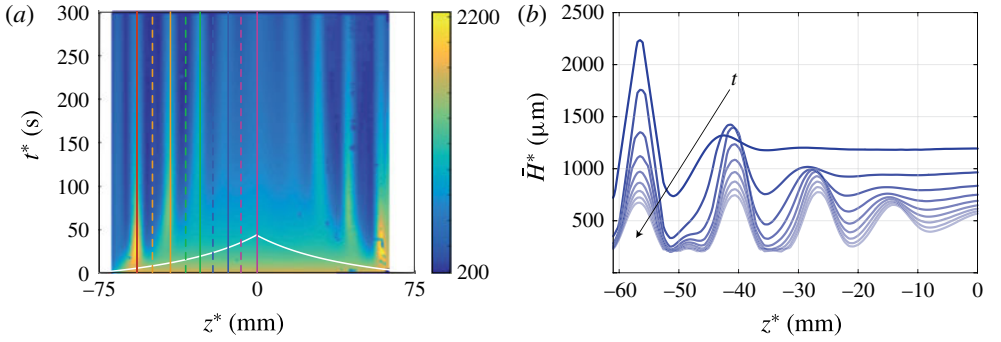

FIGURE 13. (Colour online) (*a*) Spatio-temporal diagram of the film thickness $\bar{H}^*$ measured experimentally along the cylinder generatrix at $\theta = 0$. Solid and dashed lines correspond to the locations of the peaks and valleys, respectively, whose thickness evolutions are shown in figure 14(*b*). The white line corresponds to the invading front location z_f^* predicted by the linear theory. The film thickness close to the extremities of the cylinder is not shown in the spatio-temporal diagram due to measurement uncertainties induced by the large thickness gradients. (*b*) Profiles of $\bar{H}$ at successive times $t = 30, 60, \ldots, 270$ s for a range of dimensional axial locations $z^* \in [-61, 0]$ mm. The Bond number is approximatively 67 and the film aspect ratio 0.02.

is satisfactory. In reality, rivulets grow in a finite domain whose width is not an integer multiple of the most amplified wavelength, which they progressively invade starting from the boundaries. The profiles in figure 13(*b*) are qualitatively similar to their numerical counterpart. In particular the aforementioned higher harmonics are evident in the valleys between the rivulets. The detailed evolution of film thickness along the peaks and valleys is shown in figure 14(*b*). The trend of these curves is similar to that found numerically (see figure 12*a*). Rivulets undergo a transient growth, whose magnitude decreases as we move towards the centre of the sample. The RTI propagates from the boundaries, where it is forced by a meniscus or a contact line. Limat *et al.* (1992) have shown that the front velocity of rolls predicted by the linear marginal stability criterion is given by $v_f = 0.54\,(H^*)^3(\rho g)^{3/2}/\mu\gamma^{1/2}$, corresponding to the pulled fronts of Van Saarloos (2003). Such a front velocity model would predict a linear propagation of the front position in time. In experiments the front velocity reduces with time – the white lines from linear theory as reported in figure 13(*a*) are concave up. We hypothesize that this effect is caused by drainage, which effectively lowers H^* as time goes by: $H^*(t^*) = H_i^*/\sqrt{1 + 2\,t^*/3}$. We have successfully reproduced the effect of the lateral boundaries on the inward propagation of rivulets using a periodic but inhomogeneous initial condition, as described in § 5.3.

5.3. *Numerical experiment on the front propagation of rivulets*

The experimentally observed drainage characteristics of rivulets presented in § 5.2 can be reproduced by resolving the lubrication equation (5.1) with particular boundary conditions. In order to avoid dealing with the difficult problem of a moving contact line at the boundaries, we consider periodic boundary conditions with a symmetric initial perturbation of the form $\bar{H}_0 = 1 + \varepsilon\{\exp[-(z + L_z/2)^2/(2\sigma^2)] + \exp[-(z - L_z/2)^2/(2\sigma^2)]\}$, with $\sigma = 2$ for example.

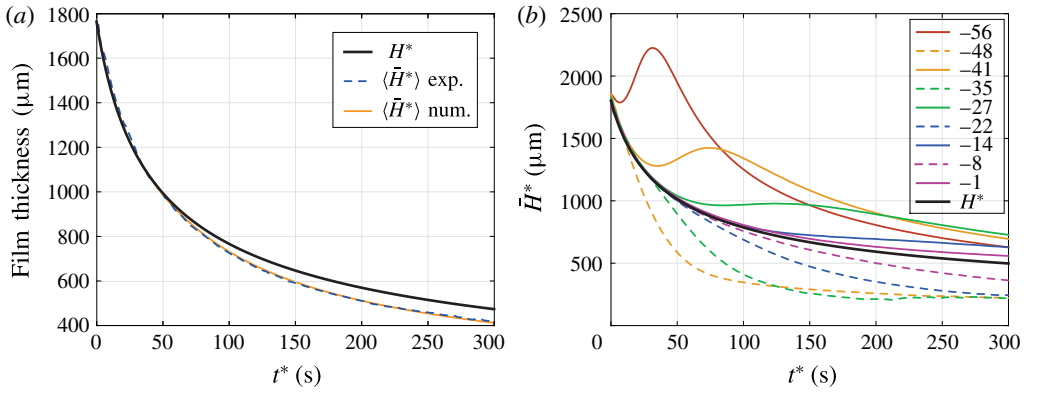

FIGURE 14. (Colour online) (*a*) Evolution of the mean film thickness $\langle \bar{H}^* \rangle$ obtained experimentally (blue dashed line) and numerically (orange thin line) compared to the uniform pure draining solution $H^*(t^*) = H_i^*/\sqrt{1+2\,t^*/3}$ (thick black solid line). (*b*) Film thickness evolutions at the peaks (solid lines) and valleys (dashed lines) of the rivulets shown in figure 13(*a*). The location in mm is shown in the legend. The thick black solid line corresponds to the pure drainage solution H^*. Here $Bo = 67$, $\delta = 0.02$, $\varepsilon = 0.01$ and $\sigma = 2$ (for numerical results, see § 5.3).

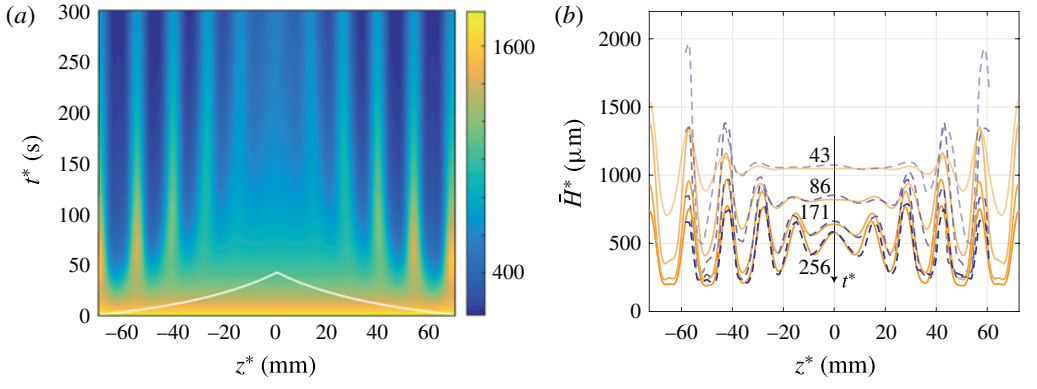

FIGURE 15. (Colour online) (*a*) Spatio-temporal diagram of the film thickness $\bar{H}^*$ obtained numerically using the initial and boundary conditions described in § 5.3. The white line corresponds to the invading front location z_f^* predicted by the linear theory. (*b*) Comparison between experimental (blue dashed line) and numerical (orange solid line) film thicknesses at different times. Here $Bo = 67$, $\delta = 0.02$, $\varepsilon = 0.01$ and $\sigma = 2$.

The spatio-temporal evolution of the film thickness for such an initial condition is displayed in figure 15(*a*). Similarly to figure 13(*a*), the rivulets first form close to the boundary and then propagate into the domain. Again, the front velocity reduces as the film becomes thinner. The linearly most amplified wavelength λ_{max}^{β} is also selected. This *ad hoc* model for the boundary conditions is able to capture the dynamics of the rivulets invading the domain (see figure 15*b*) and thus the faster drainage of the rivulets (see figure 14*a*). The initial differences, imputable to the *ad hoc* boundary conditions, do not affect the later stage of rivulet formation and invasion, making this model satisfactory.

6. Conclusions

We have investigated the RTI of thin viscous films coating the interior of a cylinder. Unlike the classic RTI under a horizontal substrate, where the most amplified pattern has a circular or hexagonal symmetry, here, the geometry of the substrate breaks the symmetry of the problem and gives rise to different patterns depending on the Bond number and the perturbations amplitude. For moderate Bond numbers ($12 < Bo \lesssim 100$) and small film aspect ratios, the thin film results into rivulets, i.e. equally spaced axial perturbations that initially grow and eventually decay due to the drainage. For $Bo \gtrsim 100$, the initially uniform film quickly destabilizes into a two-dimensional pattern of droplets, which might drip for thick coatings or are convected to the bottom of the cylinder for thinner films. We showed numerically that this transition is dependent on the amplitude of the perturbation, which precludes the determination of universal thresholds. We have rationalized our experimental phase diagram using a linear optimal transient growth analysis and nonlinear numerical simulations. The linear optimal transient growth analysis at the top of the cylinder predicts the faster growth of rivulets for moderate Bond numbers (or small perturbations) as well as the eventual asymptotic stability of the coating. The linearly most amplified wavenumber along the axial direction corresponds to the classical wavenumber $1/(\sqrt{2}\ell_c)$ of the horizontal RTI. Yet, the linear amplification does not coincide with the classical theory (Fermigier *et al.* 1992) because of the film drainage in the polar direction. For larger Bond numbers (or large perturbations), all modes experience the same linear growth so that the resulting pattern is solely selected by their nonlinear interactions. In particular, the thin film may destabilize into a two-dimensional array of droplets rather than into rivulets, as seen in our numerical simulations of the nonlinear lubrication equation. The novelty of our work lies in the proof that rivulets are the prevailing pattern at moderate Bond numbers ($12 < Bo \lesssim 100$) for thin films in cylindrical substrates. Recall that they are not dominant for the horizontal RTI. Such rivulets may induce a faster drainage (up to 20 % faster in the case under study). We have shown that this effect relies on the nonlinear interactions between the fundamental and higher-order harmonics. The more the film is perturbed, the earlier the nonlinear terms will become relevant and the faster the mean film thickness on the upper part of the cylinder will decrease. When the film aspect ratio is larger, the transition to a two-dimensional array of droplets shifts to larger Bond numbers, as found experimentally. Rivulets first form and destabilize into aligned droplets due to a secondary instability.

It should be mentioned that rivulets, defined here as structures aligned in the direction of the flow, are not intrinsic to the cylindrical geometry. Similar structures arise when totally different forces are at play. For example, Scheid *et al.* (2008) observed the formation of equally spaced rivulets aligned with the direction of the flow for thin films on a vertical heated wall when inertia effects are negligible. They also appear for a thin film above (Troian *et al.* 1989) and below (Lin, Kondic & Filippov 2012) an inclined plane or a cylinder (Takagi & Huppert 2010) in the presence of a moving contact line, or on a film falling along the outside wall of a vertical spinning cylinder (Rietz *et al.* 2017).

As a possible follow-up to this work, it would be interesting to consider a thin liquid film coating the outside of horizontal or inclined cylinders of moderate diameter. For this configuration, the drainage solution is not asymptotically stable. Reisfeld & Bankoff (1992), de Bruyn (1997) and Weidner *et al.* (1997), who considered thin films on the exterior of a horizontal cylinder, showed that the fluid accumulates at the lower external part of the cylinder and forms droplets, which grow in size and eventually

pinch off. However, the diameter of the cylinder in all these studies was too small to observe the transition from rivulets to a two-dimensional array of droplets. Mainly single droplets aligned along the axial direction were observed. For even smaller radii, the Rayleigh–Plateau instability would appear (Duclaux *et al.* 2006).

Concerning the limitations of our work, the pinching off of droplets (Eggers & Villermaux 2008) as well as the later stages of the dynamics are not considered in this study. After the rivulets have drained out and the droplets have dripped, the liquid will be mainly collected at the bottom of the cylinder and only a thin layer will remain on the upper part of the cylinder. When the corresponding Bond number becomes of the order of the film aspect ratio, we expect lobes, collars and dry spots to form, as discussed by Jensen (1997) and King *et al.* (2007) for inclined and curved cylinders.

Finally, we expect that a spherical substrate would annihilate the formation of rivulets. This is probably the key to the success of chocolatiers, who easily coat spherically shaped moulds in a uniform way (Lee *et al.* 2016).

Acknowledgements

We would like to acknowledge Laurent Limat for delightful discussions about the nonlinear analysis of the Rayleigh–Taylor instability. Also, we would like to thank L. Zhu for nicely introducing us to COMSOL Multiphysics. This work was funded by ERC Grant No. SIMCOMICS 280117. B.S. thanks the FRS-FNRS and the IAP-7/38 MicroMAST project for financial support.

Supplementary movies

Supplementary movies are available at https://doi.org/10.1017/jfm.2017.817.

Appendix A. Derivation of the lubrication equation

The derivation of the model equation presented in § 3.1 is briefly outlined here, extending to the axial direction the derivation of Balestra *et al.* (2016). Consider a thin film coating the interior of a cylinder of radius R and length L_z, as shown in figure 1. Given an initial average thickness of H_i^*, the resulting film aspect ratio reads $\delta = H_i^*/R$. The characteristic length in the radial direction is H_i^*, whereas the characteristic length in the polar and axial directions is R. The long-wavelength approximation is employed since $\delta \ll 1$ (Oron *et al.* 1997). Mass conservation indicates that the velocity normal to the interface is much smaller than the polar and axial components, $v^* \sim \delta\, u^* \ll u^*$ and $v^* \sim \delta\, w^* \ll w^*$, respectively. The Stokes equations are used, as the Reynolds number is low and inertial effects can be neglected. The momentum equation in the radial direction is

$$0 = -\frac{1}{\rho}\frac{\partial p^*}{\partial r^*} - g\cos\theta, \tag{A 1}$$

and the boundary condition for the pressure is given by $p^*(R - \bar{H}^*, \theta, z^*) = p_0^* - \gamma\bar{\kappa}^*$, where p_0^* is the external pressure, γ the surface tension and $\bar{\kappa}^*$ the curvature of the interface. Equation (A 1) can be integrated along the radial direction, and, using the aforementioned boundary condition, one obtains the pressure distribution $p^*(r^*, \theta, z^*) = p_0^* - \gamma\bar{\kappa}^* + \rho g\cos\theta\,(R - \bar{H}^* - r^*)$. The θ and z^* components of the momentum equation read

$$0 = -\frac{1}{\rho r^*}\frac{\partial p^*}{\partial \theta} + \nu\left[\frac{\partial}{\partial r^*}\left(\frac{1}{r^*}\frac{\partial}{\partial r^*}\left(r^* u^*\right)\right) + \frac{1}{r^{*2}}\frac{\partial^2 u^*}{\partial \theta^2} + \frac{\partial^2 u^*}{\partial z^{*2}}\right] + g\sin\theta, \tag{A 2}$$

$$0 = -\frac{1}{\rho}\frac{\partial p^*}{\partial z^*} + \nu\left[\frac{1}{r^*}\frac{\partial}{\partial r^*}\left(r^*\frac{\partial w^*}{\partial r^*}\right) + \frac{1}{r^{*2}}\frac{\partial^2 w^*}{\partial \theta^2} + \frac{\partial^2 w^*}{\partial z^{*2}}\right]. \tag{A 3}$$

With the change of variable $r^* = R - s$, where $0 \leqslant s \leqslant \bar{H}^* \ll R$, the viscous terms in (A 2) and (A 3) reduce to $\nu\partial^2 u^*/\partial s^2$ and $\nu\partial^2 w^*/\partial s^2$, respectively, plus terms at least an order δ smaller. Keeping the dominant order of the viscous term, as well as the surface tension and gravitational terms, equations (A 2) and (A 3) with the expression for p^* become

$$0 = \frac{\gamma\bar{\kappa}^*_\theta}{\rho R} + \frac{g\cos\theta\,\bar{H}^*_\theta}{R} + \nu\frac{\partial^2 u^*}{\partial s^2} + g\sin\theta, \tag{A 4}$$

$$0 = \frac{\gamma\bar{\kappa}^*_{z^*}}{\rho} + g\cos\theta\,\bar{H}^*_{z^*} + \nu\frac{\partial^2 w^*}{\partial s^2}. \tag{A 5}$$

Equations (A 4) and (A 5) can be integrated twice, and considering the zero-slip boundary condition at the cylinder surface, $u^*(0,\theta,z^*) = 0$ and $w^*(0,\theta,z^*) = 0$, as well as the zero-shear-stress interface, $\partial u^*(\bar{H}^*,\theta,z^*)/\partial s = 0$ and $\partial w^*(\bar{H}^*,\theta,z^*)/\partial s = 0$, yields the velocity components:

$$u^*(s,\theta,z^*) = \left(\frac{\gamma\bar{\kappa}^*_\theta}{\mu R} + \frac{\rho g\cos\theta\,\bar{H}^*_\theta}{\mu R} + \frac{\rho g\sin\theta}{\mu}\right)\left(\bar{H}^* - \frac{s}{2}\right)s, \tag{A 6}$$

$$w^*(s,\theta,z^*) = \left(\frac{\gamma\bar{\kappa}^*_{z^*}}{\mu} + \frac{\rho g\cos\theta\,\bar{H}^*_{z^*}}{\mu}\right)\left(\bar{H}^* - \frac{s}{2}\right)s. \tag{A 7}$$

The flow rate in the polar direction is given by $Q^\theta(\theta,z^*) = \int_0^{\bar{H}^*} u^*(s,\theta,z^*)\,\mathrm{d}s$ and in the axial direction by $Q^{z^*}(\theta,z^*) = \int_0^{\bar{H}^*} w^*(s,\theta,z^*)\,\mathrm{d}s$. Mass conservation in cylindrical coordinates, $\partial\bar{H}^*/\partial t^* + R^{-1}\partial Q^\theta/\partial\theta + \partial Q^{z^*}/\partial z^* = 0$, yields the lubrication equation:

$$\bar{H}^*_{t^*} + \frac{1}{3\mu R}\left[\bar{H}^{*3}\left(\underbrace{\frac{\gamma\bar{\kappa}^*_\theta}{R}}_{\mathrm{I}} + \underbrace{\frac{\rho g\cos\theta\,\bar{H}^*_\theta}{R}}_{\mathrm{II}} + \underbrace{\rho g\sin\theta}_{\mathrm{III}}\right)\right]_\theta + \frac{1}{3\mu}\left[\bar{H}^{*3}\left(\underbrace{\gamma\bar{\kappa}^*_{z^*}}_{\mathrm{I}} + \underbrace{\rho g\cos\theta\,\bar{H}^*_{z^*}}_{\mathrm{II}}\right)\right]_{z^*} = 0. \tag{A 8}$$

The term I in the spatial variation of the flux corresponds to the surface tension effects, term II to the variation of the hydrostatic pressure distribution and term III to the drainage.

The free surface of the viscous film is defined by

$$F(r^*,\theta,z^*,t^*) = r^* - [R - \bar{H}^*(\theta,z^*,t^*)] = 0, \tag{A 9}$$

and its normal vector $\boldsymbol{n}$ is given by

$$\boldsymbol{n} = \frac{\nabla F}{\|\nabla F\|} = \frac{\left[1, \dfrac{\bar{H}^*_\theta}{r^*}, \bar{H}^*_{z^*}\right]^{\mathrm{T}}}{\sqrt{1 + \left(\dfrac{\bar{H}^*_\theta}{r^*}\right)^2 + \left(\bar{H}^*_{z^*}\right)^2}} \tag{A 10}$$

at $r^* = R - \bar{H}^*$. The interfacial curvature therefore reads

$$\begin{aligned}\bar{\kappa}^* = \nabla \cdot \boldsymbol{n} \;=\; & -\frac{\bar{H}^*_{z^*z^*}\bar{H}^{*2}_{z^*}}{\left(\dfrac{\bar{H}^{*2}_\theta}{r^{*2}} + \bar{H}^{*2}_{z^*} + 1\right)^{3/2}} - \frac{2\bar{H}^*_\theta \bar{H}^*_{\theta z^*}\bar{H}^*_{z^*}}{r^{*2}\left(\dfrac{\bar{H}^{*2}_\theta}{r^{*2}} + \bar{H}^{*2}_{z^*} + 1\right)^{3/2}} \\ & + \frac{\bar{H}^*_{\theta\theta}}{r^{*2}\sqrt{\dfrac{\bar{H}^{*2}_\theta}{r^{*2}} + \bar{H}^{*2}_{z^*} + 1}} + \frac{\bar{H}^*_{z^*z^*}}{\sqrt{\dfrac{\bar{H}^{*2}_\theta}{r^{*2}} + \bar{H}^{*2}_{z^*} + 1}} \\ & + \frac{1}{r^*\sqrt{\dfrac{\bar{H}^{*2}_\theta}{r^{*2}} + \bar{H}^{*2}_{z^*} + 1}} - \frac{\bar{H}^{*2}_\theta \bar{H}^*_{\theta\theta}}{r^{*4}\left(\dfrac{\bar{H}^{*2}_\theta}{r^{*2}} + \bar{H}^{*2}_{z^*} + 1\right)^{3/2}} \\ & + \frac{\bar{H}^{*2}_\theta}{r^{*3}\left(\dfrac{\bar{H}^{*2}_\theta}{r^{*2}} + \bar{H}^{*2}_{z^*} + 1\right)^{3/2}}\end{aligned} \tag{A 11}$$

at $r^* = R - \bar{H}^*$.

Lengths can be non-dimensionalized by the initial average film thickness H^*_i and the time by the gravitational relaxation scale $\mu R/(\rho g H^{*2}_i)$, so that the lubrication equation expressed with non-dimensional quantities finally reads

$$\bar{H}_t + \frac{1}{3}\left[\bar{H}^3\left(\underbrace{\frac{1}{Bo}\bar{\kappa}_\theta}_{\mathrm{I}} + \underbrace{\delta\bar{H}_\theta\cos\theta}_{\mathrm{II}} + \underbrace{\sin\theta}_{\mathrm{III}}\right)\right]_\theta + \frac{1}{3\delta^2}\left[\bar{H}^3\left(\underbrace{\frac{1}{Bo}\bar{\kappa}_z}_{\mathrm{I}} + \underbrace{\delta\bar{H}_z\cos\theta}_{\mathrm{II}}\right)\right]_z = 0, \tag{A 12}$$

where $Bo = \rho g H^*_i R/\gamma$ is the modified Bond number.

The curvature up to the second order in δ is

$$\begin{aligned}\bar{\kappa} \;=\; & \frac{\bar{H}_{zz}}{(\bar{H}^2_z + 1)^{3/2}} + \frac{\delta}{(\bar{H}^2_z + 1)^{1/2}} \\ & - \delta^2\left[\frac{\bar{H}_{zz}\bar{H}^2_\theta}{2(\bar{H}^2_z + 1)^{3/2}} - \frac{3\bar{H}^2_z\bar{H}_{zz}\bar{H}^2_\theta}{2(\bar{H}^2_z + 1)^{5/2}} + \frac{2\bar{H}_z\bar{H}_{\theta z}\bar{H}_\theta}{(\bar{H}^2_z + 1)^{3/2}} - \frac{\bar{H}_{\theta\theta}}{(\bar{H}^2_z + 1)^{1/2}} - \frac{\bar{H}}{(\bar{H}^2_z + 1)^{1/2}}\right] \\ & + O(\delta^3).\end{aligned} \tag{A 13}$$

A more sophisticated model could be employed to consider higher-order curvature terms and larger film aspect ratios, as done by Weidner *et al.* (1997).

Appendix B. Lubrication equation for small angles

The lubrication equation (A 12) can be further simplified if one considers the limit of small angles θ. Following Trinh *et al.* (2014), the change of variable $\theta = \delta^{1/2}x$ and $z = \delta^{-1/2}y$ can employed when $\delta \ll 1$. The curvature becomes $\bar{\kappa} = \delta(1 + \bar{H}_{xx} + \bar{H}_{yy}) + O(\delta^2)$ so that (A 12) reads, using $\cos\theta \approx 1$ and $\sin\theta \approx \theta = \delta^{1/2}x$:

$$\bar{H}_t + \frac{\delta^{-1/2}}{3}\left[\bar{H}^3\left(\frac{\delta\delta^{-1/2}}{Bo}\left(\bar{H}_{xxx} + \bar{H}_{yyx}\right) + \delta\delta^{-1/2}\bar{H}_x + \delta^{1/2}x\right)\right]_x + \frac{\delta^{1/2}}{3\delta^2}\left[\bar{H}^3\left(\frac{\delta\delta^{1/2}}{Bo}\left(\bar{H}_{xxy} + \bar{H}_{yyy}\right) + \delta\delta^{1/2}\bar{H}_y\right)\right]_y = 0. \tag{B 1}$$

The resulting equation, which can be rewritten as

$$\bar{H}_t + \boldsymbol{\nabla}\cdot\left[\frac{\bar{H}^3}{3}\boldsymbol{\nabla}\left(\frac{1}{Bo}\nabla^2\bar{H} + \bar{H} + \frac{x^2}{2}\right)\right] = 0, \tag{B 2}$$

with $\boldsymbol{\nabla} = [\partial_x, \partial_y]^{\mathrm{T}}$ as the gradient operator, is independent of the aspect ratio and the Bond number is the only remaining parameter. Equation (B 2) is the planar thin-film equation of Fermigier *et al.* (1992) with an additional polar flux term proportional to the distance from the uppermost generatrix.

Appendix C. Derivation of the drainage solution

For an initial uniform profile $H(x, y, 0) = 1$, the film thickness will remain uniform close to the top of the cylinder. Equation (B 2) becomes

$$H_t + \frac{H^3}{3} = 0, \tag{C 1}$$

whose solution with the unitary initial profile is the drainage solution (Takagi & Huppert 2010; Trinh *et al.* 2014)

$$H(t) = \frac{1}{\sqrt{1 + \frac{2}{3}t}}. \tag{C 2}$$

It has to be pointed out that, by employing the full lubrication equation (A 12) and under the assumption of small deformations, i.e. neglecting surface tension and hydrostatic pressure effects, the lubrication equation would be

$$H_t + \tfrac{1}{3}(H^3\sin\theta)_\theta = 0. \tag{C 3}$$

Equation (C 3) can be resolved analytically by a regular perturbation expansion around $\theta = 0$ as explained in Lee *et al.* (2016) for the drainage on a sphere. The same cannot be done starting from (B 2), as it requires terms in θ^2 to be kept in the equation. Eventually, the first spatial correction to the drainage solution from a uniform initial condition reads

$$H(t, \theta) = \frac{1}{\sqrt{1 + \frac{2}{3}t}}\left[1 + \frac{\theta^2}{16}\left(1 - \frac{1}{(1 + \frac{2}{3}t)^4}\right)\right] + O(\theta^4). \tag{C 4}$$

We have found that this solution is accurate at least up to $\pi/6$ and the largest error with respect to the numerical resolution of the full lubrication equation (A 12) is within 2.5 % at $\pi/2$. Finally, as the first correction is at second order in space, θ^2, considering a uniform drainage solution is a valid assumption for the region close to the top of the cylinder (see figure 16*a*).

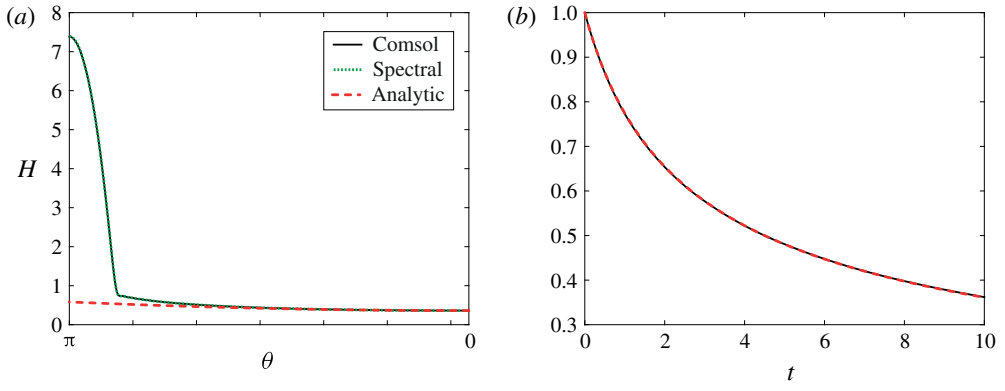

FIGURE 16. (Colour online) (*a*) Polar dependence of the film thickness profile at $z=0$ for $t=10$ obtained by the two-dimensional numerical resolution with COMSOL Multiphysics (solid line) and by the numerical resolution of the one-dimensional lubrication equation in θ with a spectral code (dotted green line) (Balestra *et al.* 2016). The dashed red line corresponds to spatial variation of drainage solution given by (C 4). (*b*) Film thickness evolution at $\theta=0$ obtained by the two-dimensional numerical resolution with COMSOL Multiphysics (solid line) and analytical prediction H given by (3.4) (dashed line). Here $Bo=100$ and $\delta=0.01$.

Appendix D. Numerical methods

D.1. *Two-dimensional simulations*

For the numerical resolution of the two-dimensional lubrication equation (3.1), we employed COMSOL Multiphysics, which uses a finite element method. Cubic elements with Lagrangian shape functions are employed on a free triangular grid with characteristic size of 0.8. The film thickness $\bar{H}$ as well as the curvature $\bar{\kappa}$ are the two resolved variables.

The obtained film thickness at $\theta=0$ and at $z=0$ for an initially uniform profile are compared to the analytical result H and to an in-house one-dimensional spectral code (Balestra *et al.* 2016) in figure 16. The comparison for initially forced rivulets is shown in figure 10(*b*). In view of the very good agreement, the choice for the use of COMSOL Multiphysics to solve for the lubrication equation in two dimensions follows naturally. Other options would be the implementation of an ADI method (Witelski & Bowen 2003) such as the one employed by Weidner *et al.* (1997) or Lister *et al.* (2010).

D.2. *One-dimensional simulations*

The lubrication equation (5.1) is discretized with a central finite difference scheme and evolved in time with the second-order Crank–Nicolson MATLAB routine `ode23t.m` to avoid numerical diffusion. The axial range is uniformly discretized with N collocation points, giving a grid spacing typically of approximately 0.03 for $N=500$. The convergence study for a typical parameter set is shown in figure 17.

Appendix E. Confocal chromatic imaging technique

The principle of the confocal chromatic imaging technique is the following. An achromatic lens decomposes the incident white light into a continuum of

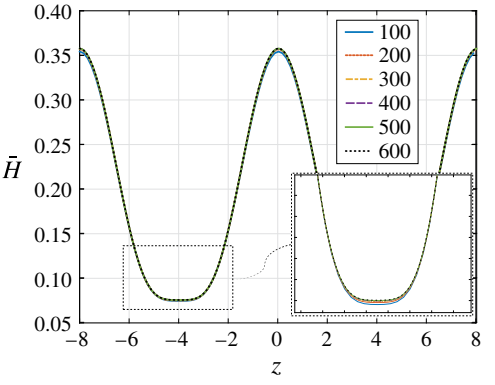

FIGURE 17. (Colour online) Convergence study for the nonlinear evolution of rivulets initially perturbed with b_0 for $Bo = 70$, $\delta = 0.02$, $\varepsilon = 10^{-2}$ and $t = 20$. The number of collocation points N is shown in the legend.

monochromatic images, which constitutes the measurement range. The light reflected by a sample surface put inside this range is collected by a beam splitter. A pinhole then allows one to block the defocused light that does not come from the sample surface. Eventually, the spectral repartition of the collected light is analysed by a spectrometer. The wavelength of maximum intensity is detected and the distance value is deduced from a calibration curve. Several reflecting interfaces can be detected at the same time, allowing thickness measurement of thin transparent layers. When mounted onto a linear translation stage, the spatial resolution depends on the measurement frequency and speed of the translation stage.

REFERENCES

ABDELALL, F. F., ABDEL-KHALIK, S. I., SADOWSKI, D. L., SHIN, S. & YODA, M. 2006 On the Rayleigh–Taylor instability for confined liquid films with injection through the bounding surfaces. *Intl J. Heat Mass Transfer* **49** (7), 1529–1546.

ALEKSEENKO, S. V., AKTERSHEV, S. P., BOBYLEV, A. V., KHARLAMOV, S. M. & MARKOVICH, D. M. 2015 Nonlinear forced waves in a vertical rivulet flow. *J. Fluid Mech.* **770**, 350–373.

ALEXEEV, A. & ORON, A. 2007 Suppression of the Rayleigh–Taylor instability of thin liquid films by the Marangoni effect. *Phys. Fluids* **19** (8), 082101.

BABCHIN, A. J., FRENKEL, A. L., LEVICH, B. G. & SIVASHINSKY, G. I. 1983 Nonlinear saturation of Rayleigh–Taylor instability in thin films. *Phys. Fluids* **26** (11), 3159–3161.

BALESTRA, G., BRUN, P.-T. & GALLAIRE, F. 2016 Rayleigh–Taylor instability under curved substrates: an optimal transient growth analysis. *Phys. Rev. Fluids* **1** (8), 083902.

BENILOV, E. S. & LAPIN, V. N. 2013 Inertial instability of flows on the inside or outside of a rotating horizontal cylinder. *J. Fluid Mech.* **736**, 107–129.

BOOS, W. & THESS, A. 1999 Cascade of structures in long-wavelength Marangoni instability. *Phys. Fluids* **11** (6), 1484–1494.

BRUN, P.-T., DAMIANO, A., RIEU, P., BALESTRA, G. & GALLAIRE, F. 2015 Rayleigh–Taylor instability under an inclined plane. *Phys. Fluids* **27** (8), 084107.

DE BRUYN, J. R. 1997 Crossover between surface tension and gravity-driven instabilities of a thin fluid layer on a horizontal cylinder. *Phys. Fluids* **9** (6), 1599–1605.

BURGESS, J. M., JUEL, A., MCCORMICK, W. D., SWIFT, J. B. & SWINNEY, H. L. 2001 Suppression of dripping from a ceiling. *Phys. Rev. Lett.* **86** (7), 1203–1206.

CHANDRASEKHAR, S. 1981 *Hydrodynamic and Hydromagnetic Stability*. Dover.

CIMPEANU, R., PAPAGEORGIOU, D. T. & PETROPOULOS, P. G. 2014 On the control and suppression of the Rayleigh–Taylor instability using electric fields. *Phys. Fluids* **26** (2), 022105.

DUCLAUX, V., CLANET, C. & QUÉRÉ, D. 2006 The effects of gravity on the capillary instability in tubes. *J. Fluid Mech.* **556**, 217–226.

EGGERS, J. & VILLERMAUX, E. 2008 Physics of liquid jets. *Rep. Prog. Phys.* **71** (3), 036601.

FAUVE, S. 2005 Pattern forming instabilities. In *Hydrodynamics and Nonlinear Instabilities* (ed. C. Godrèche & P. Manneville), chap. 4, pp. 387–491. Cambridge University Press.

FERMIGIER, M., LIMAT, L., WESFREID, J. E., BOUDINET, P. & QUILLIET, C. 1992 Two-dimensional patterns in Rayleigh–Taylor instability of a thin layer. *J. Fluid Mech.* **236**, 349–383.

GALLAIRE, F. & BRUN, P.-T. 2017 Fluid dynamic instabilities: theory and application to pattern forming in complex media. *Phil. Trans. R. Soc. Lond.* A **375** (2093), 20160155.

HAMMOND, P. S. 1983 Nonlinear adjustment of a thin annular film of viscous fluid surrounding a thread of another within a circular cylindrical pipe. *J. Fluid Mech.* **137**, 363–384.

HOSOI, A. E. & MAHADEVAN, L. 1999 Axial instability of a free-surface front in a partially filled horizontal rotating cylinder. *Phys. Fluids* **11** (1), 97–106.

INDEIKINA, A., VERETENNIKOV, I. & CHANG, H.-C. 1997 Drop fall-off from pendent rivulets. *J. Fluid Mech.* **338**, 173–201.

JENSEN, O. E. 1997 The thin liquid lining of a weakly curved cylindrical tube. *J. Fluid Mech.* **331**, 373–403.

KAITA, R., BERZAK, L., BOYLE, D., GRAY, T., GRANSTEDT, E., HAMMETT, G., JACOBSON, C. M., JONES, A., KOZUB, T., KUGEL, H. & OTHERS 2010 Experiments with liquid metal walls: status of the lithium tokamak experiment. *Fusion Engng Des.* **85** (6), 874–881.

KING, A. A., CUMMINGS, L. J., NAIRE, S. & JENSEN, O. E. 2007 Liquid film dynamics in horizontal and tilted tubes: dry spots and sliding drops. *Phys. Fluids* **19** (4), 042102.

KOFMAN, N., RUYER-QUIL, C. & MERGUI, S. 2016 Selection of solitary waves in vertically falling liquid films. *Intl J. Multiphase Flow* **84**, 75–85.

LAPUERTA, V., MANCEBO, F. J. & VEGA, J. M. 2001 Control of Rayleigh–Taylor instability by vertical vibration in large aspect ratio containers. *Phys. Rev.* E **64** (1), 016318.

LEE, A., BRUN, P.-T., MARTHELOT, J., BALESTRA, G., GALLAIRE, F. & REIS, P. M. 2016 Fabrication of slender elastic shells by the coating of curved surfaces. *Nat. Commun.* **7**, 11155.

LIMAT, L. 1993 Instabilité d'un liquide suspendu sous un surplomb solide: influence de l'épaisseur de la couche. *C. R. Acad. Sci. Paris* **317** (5), 563–568.

LIMAT, L., JENFFER, P., DAGENS, B., TOURON, E., FERMIGIER, M. & WESFREID, J. E. 1992 Gravitational instabilities of thin liquid layers: dynamics of pattern selection. *Physica* D **61** (1), 166–182.

LIN, T.-S., KONDIC, L. & FILIPPOV, A. 2012 Thin films flowing down inverted substrates: three-dimensional flow. *Phys. Fluids* **24** (2), 022105.

LISTER, J. R., RALLISON, J. M., KING, A. A., CUMMINGS, L. J. & JENSEN, O. E. 2006 Capillary drainage of an annular film: the dynamics of collars and lobes. *J. Fluid Mech.* **552**, 311–343.

LISTER, J. R., RALLISON, J. M. & REES, S. J. 2010 The nonlinear dynamics of pendent drops on a thin film coating the underside of a ceiling. *J. Fluid Mech.* **647**, 239–264.

MANTIČ-LUGO, V., ARRATIA, C. & GALLAIRE, F. 2014 Self-consistent mean flow description of the nonlinear saturation of the vortex shedding in the cylinder wake. *Phys. Rev. Lett.* **113** (8), 084501.

MAUREL, A., PAGNEUX, V. & WESFREID, J. E. 1995 Mean-flow correction as non-linear saturation mechanism. *Europhys. Lett.* **32** (3), 217.

MELO, F. 1993 Localized states in a film-dragging experiment. *Phys. Rev.* E **48** (4), 2704.

ORON, A., DAVIS, S. H. & BANKOFF, S. G. 1997 Long-scale evolution of thin liquid films. *Rev. Mod. Phys.* **69** (3), 931.

ORON, A. & ROSENAU, P. 1989 Nonlinear evolution and breaking of interfacial Rayleigh–Taylor waves. *Phys. Fluids* A **1** (7), 1155–1165.

POUGATCH, K. & FRIGAARD, I. 2011 Thin film flow on the inside surface of a horizontally rotating cylinder: steady state solutions and their stability. *Phys. Fluids* **23** (2), 022102.

RAYLEIGH, LORD 1882 Investigation of the character of the equilibrium of an incompressible heavy fluid of variable density. *Proc. Lond. Math. Soc.* **s1–14** (1), 170–177.

REISFELD, B. & BANKOFF, S. G. 1992 Non-isothermal flow of a liquid film on a horizontal cylinder. *J. Fluid Mech.* **236**, 167–196.

RIETZ, M., SCHEID, B., GALLAIRE, F., KOFMAN, N., KNEER, R. & ROHLFS, W. 2017 Dynamics of falling films on the outside of a vertical rotating cylinder: waves, rivulets and dripping transitions. *J. Fluid Mech.* **832**, 189–211.

ROHLFS, W., PISCHKE, P. & SCHEID, B. 2017 Hydrodynamic waves in films flowing under an inclined plane. *Phys. Rev. Fluids* **2** (4), 044003.

SCHEID, B., KALLIADASIS, S., RUYER-QUIL, C. & COLINET, P. 2008 Interaction of three-dimensional hydrodynamic and thermocapillary instabilities in film flows. *Phys. Rev.* E **78** (6), 066311.

SCHEID, B., KOFMAN, N. & ROHLFS, W. 2016 Critical inclination for absolute/convective instability transition in inverted falling films. *Phys. Fluids* **28** (4), 044107.

SEIDEN, G. & THOMAS, P. J. 2011 Complexity, segregation, and pattern formation in rotating-drum flows. *Rev. Mod. Phys.* **83**, 1323–1365.

SHARP, D. H. 1984 An overview of Rayleigh–Taylor instability. *Physica* D **12** (1–3), 3–18.

TAKAGI, D. & HUPPERT, H. E. 2010 Flow and instability of thin films on a cylinder and sphere. *J. Fluid Mech.* **647**, 221.

TAYLOR, G. 1950 The instability of liquid surfaces when accelerated in a direction perpendicular to their planes. I. *Proc. R. Soc. Lond.* A **201** (1065), 192–196.

THORODDSEN, S. T. & MAHADEVAN, L. 1997 Experimental study of coating flows in partially-filled horizontally rotating cylinder. *Exp. Fluids* **23**, 1–13.

TRINH, P. H., KIM, H., HAMMOUD, N., HOWELL, P. D., CHAPMAN, S. J. & STONE, H. A. 2014 Curvature suppresses the Rayleigh–Taylor instability. *Phys. Fluids* **26** (5), 051704.

TROIAN, S. M., HERBOLZHEIMER, E., SAFRAN, S. A. & JOANNY, J. F. 1989 Fingering instabilities of driven spreading films. *Europhys. Lett.* **10** (1), 25.

VAN SAARLOOS, W. 2003 Front propagation into unstable states. *Phys. Rep.* **386** (2), 29–222.

WEIDNER, D. E. 2012 The effect of surfactant convection and diffusion on the evolution of an axisymmetric pendant droplet. *Phys. Fluids* **24** (6), 062104.

WEIDNER, D. E., SCHWARTZ, L. W. & ERES, M. H. 1997 Simulation of coating layer evolution and drop formation on horizontal cylinders. *J. Coll. Int. Sci.* **187** (1), 243–258.

WEIDNER, D. E., SCHWARTZ, L. W. & ERES, M. H. 2007 Suppression and reversal of drop formation in a model paint film. *Chem. Prod. Process Model.* **2** (3), 19.

WITELSKI, T. P. & BOWEN, M. 2003 ADI schemes for higher-order nonlinear diffusion equations. *App. Num. Math.* **45** (2), 331–351.

YIANTSIOS, S. G. & HIGGINS, B. G. 1989 Rayleigh–Taylor instability in thin viscous films. *Phys. Fluids* A **1** (9), 1484–1501.